Measuring the gain of a photomultiplier tube

Audrey MacLeod

Masters of Science

Physics Department

McGill University

Montreal, Québec, Canada

2007-12-21

A thesis submitted to the Faculty of Graduate Studies and Research in partial fulfilment of the requirements for the degree of Master of Science

DEDICATION

This thesis is dedicated to my mother.

ACKNOWLEDGEMENTS

I would like to thank my supervisor David Hanna for his guidance through all stages of my thesis. I also thank Ken Ragan, Luis Valcarcel and Paul Mercure for help in setting up my experiment and Micheal McCutcheon, Andrew McCann, Roxanne Guenette and Gernot Maier for help in data-analysis. I would also like to thank my father, sister and brother for their support.

ABSTRACT

Photomultiplier tubes (PMTs) are used to detect light that comes from gamma-ray initiated showers in the earth's atmosphere. The gain of the PMTs are key to determining the amount of light detected and subsequently, the energy of the incoming gamma ray. In this thesis, a new method of measuring the gain of a PMT is proposed. It relates the PMT gain to the variance of the PMT signal divided by the average current. The new method is mathematically motivated, tested with a series of experiments, and verified using simulations. In addition, it is compared with an existing method of measuring the gain. The new method is shown to be able to predict the gain to within a constant of multiplication. This constant is intrinsic to each PMT but varies from one PMT to another.

ABRÉGÉ

Les tubes photomultiplicateurs (TPM) sont utilisés pour détecter les photons qui proviennent des cascades électromagnétiques produites par les rayons gamma dans l'atmosphère terrestre. Le gain des tubes est un élément clé pour déterminer la quantité de photons détectés et par consequent, l'énergie provenant du rayon gamma. Dans cette thèse, une nouvelle méthode de mesure du gain d'un TPM est proposée. Elle relie le gain du tube à la variance du signal de celui-ci, divisé par le courant moyen. Cette nouvelle méthode, motivée mathématiquement, a été testée par une séries d'expériences et vérifiée par des simulations numériques. De plus, cette méthode a été comparée à une autre déjà existante. La nouvelle méthode s'est avérée en mesure de prédire le gain à une constante de multiplication près. Cette constante est intrinsèque à chaque tube et varie d'un à l'autre.

TABLE OF CONTENTS

LIST OF TABLES

LIST OF FIGURES

CHAPTER 1
Introduction

1.1 Cosmic Radiation

In 1912, Victor Hess discovered cosmic rays during a series of balloon flights. Nearly a hundred years later, the origin of cosmic rays remains a mystery [1]. Cosmic rays cover a wide range of energies (up to 10^{20} eV) and are created by powerful accelerators. Their energy density is about 1 eVcm^{-3}, which is comparable to the energy contained in the galactic magnetic field and in the cosmic microwave background radiation (CMBR). The sources that produce cosmic rays have a total luminosity greater than 10^{41} ergs s^{-1} [8]. Cosmic rays represent the largest source of material reaching the Earth from outside the Solar System [2]. A reasonably detailed understanding of their acceleration, propagation and production mechanisms exists at low and moderate energies, MeV and GeV [9]. However, for energies beyond 10^{12} eV, (1 TeV), their production and acceleration mechanisms are unknown [2]. Cosmic rays are energetic particles, originating in outer space. Some examples of cosmic rays are protons, helium nuclei and electrons. Charged cosmic rays are deflected by the galactic magnetic field and cannot be traced back to their origin. Neutral particle detection (gamma ray and neutrino) is key to identifying cosmic ray sources [2], assuming gamma rays come from the same sources.

1.2 Scientific Motivation for Cosmic Ray Astronomy

Our universe is dominated by objects that emit via thermal processes. These produce the black body spectra of the CMB and stars. Weekes[1] , calls this the ordinary universe. There also exists a non-thermal, extraordinary, relativistic universe which is important. Observation of the extraordinary universe at low energies is difficult since it is dominated by thermal foreground radiation. The hard power-law spectrum of many non-thermal emissions means that it makes sense to look at the high-energy radiation emitted to probe the processes [1]. In the high-energy regime, the energies of the accelerated particles surpass the energies of the largest particle accelerators on earth. The accelerated particles offer a unique laboratory for physics. High-energy particle acceleration may also occur in situations where conventional physics operates under extreme conditions, in intense gravitational and/or magnetic fields. Possibly, instead of conventional physics, new physics may be occurring [2]. The very high-energy radiation produced can be used to probe some of the more exotic properties of the universe. Dark matter searches are such an example. By looking at high energy photons, one expects to encounter new phenomena that are not observed at other wavelengths [10].

[1] Weekes is a senior astrophysicist at the Harvard-Smithsonian Center for Astrophysics and is the author of the book *Very High Energy Gamma-Ray Astronomy.*

Gamma rays can be used as probes of interstellar radiation fields, which are poorly understood. Gamma rays interact with soft photons to produce electron-positron pairs: TeV gamma rays pair-produce off infrared (IR) light of 1-10 micrometer wavelengths. The flux from a TeV gamma-ray source is attenuated by an amount that depends on the gamma-ray energy, the distance to the source and the density of intergalactic IR photons. Multiple observations of similar sources at different redshifts would provide us with the intrinsic source spectra, and allow us to estimate the IR density [2].

1.3 Cosmic Ray Production

Cosmic ray production by shock acceleration in supernovae was proposed by Enrico Fermi [11]. It offers a plausible explanation for the production of cosmic rays with energies below 10^{14} eV [12, 13, 14]. In his model, the particles are accelerated at a shock front resulting from material ejected at supersonic speeds from a supernova. The charged particles scatter off the magnetic field irregularities, and diffuse back and forth across the shock. The velocity distribution of the scattering centers on either side of the shock is isotropic such that the particles are travelling in random directions relative to the shock front in. Each passage through the shock accelerates them, ultimately leading to a net acceleration in the direction of the shock front. This process continues as long as the particles are contained in the area surrounding the shock front. The containment time is inversely proportional to the energy of the particle, which leads to a power law energy spectrum: $\frac{dN}{dE} \propto E^{-\alpha}$ [2]. For strong shocks, the power law spectral index, α, is around 2 [15].

There is also good evidence supporting particle acceleration by shock waves in a number of other astrophysical situations (solar flares, planet bow shocks etc.). The theory is also appealing from the point of view of energetics. A supernova explosion typically releases 10^{51} ergs of kinetic energy and occurs every few decades in the galaxy. Thus, the average power injected into the interstellar medium is about 10^{42} ergs s^{-1}. Supernovae could power the cosmic rays if around 10 % of the gravitational potential energy released in the collapse of a massive star went into accelerating protons and nuclei. But there is as yet no direct evidence that this theory is correct [2].

Direct evidence of Fermi shock acceleration could come from observing gamma rays emitted by these sources. Gamma rays are produced in secondary interactions involving charged particles. The production mechanism involves the acceleration of charged particles which can either be leptonic (electrons) or hadronic (protons and light nuclei). Relativistic electrons interact with ambient radiation fields via the inverse-Compton effect to produce gamma rays, whereas the collision of hadrons with matter produces secondary pions which decay to gamma rays ($\pi^0 \rightarrow \gamma\gamma$) and neutrinos ($\pi^{\pm} \rightarrow \mu \pm \nu$) [2]. Theoretical estimates for the resultant gamma ray fluxes have been made [15]. No gamma rays have yet been detected coming from supernova remnants where neutral pion production is a part of the acceleration mechanism [2].

There remains considerable speculation regarding the origin of cosmic rays with energies exceeding 10^{17} eV [2]. The maximum particle energy can be inferred from the lifetime of the shock, which weakens as it expands. A typical estimate for this maximum particle energy is $Z \times 10^{14}$ eV, where Z is the particle charge [16]. Other

more exotic scenarios like multiple supernovas or a supernova explosion in a compact binary star [17] can increase this number by 2 orders of magnitude but no further [2]. Thus this cannot explain the origin of particles with energies that exceed 10^{17} eV. It is generally believed that sources of such high-energy particles must be extra-galactic in nature since objects within our galaxy do not have the combination of size and magnetic field strength that would be necessary to contain a particle at these high energies [18]; they would leak out of the acceleration before attaining such energies.

1.4 Gamma Rays Energy Bands

Before describing the history of gamma-ray astronomy, it makes sense to define the different energy ranges that are important. The term gamma ray applies to photons with energies ranging from about 100 keV to over 100 EeV (1EeV = 10^{18} eV), which represents 15 decades in energy. Consequently, a wide variety of techniques are used to detect them. Gamma-ray energy bands are defined by the interaction techniques used in their detection (Table 1-1). They are the Medium Energy (ME) region which spans from 1 to 30 MeV, the High Energy (HE) band which spans from 30 MeV to 100 GeV, the Very High Energy (VHE) band which spans from 100 GeV to 100 TeV and the Ultra High Energy (UH) region which extends beyond 100 TeV. In the ME region, the Compton scattering process is the dominant interaction process for photons and Compton telescopes are used in their detection. Alternatively, HE and VHE use pair-production to detect photons. HE employs balloon and satellite detectors, whereas VHE relies on detecting the electromagnetic cascade initiated by gamma rays entering the Earth's atmosphere [1].

Table 1.1. Gamma-ray bands.

Band	Low/medium	High	Very High	Ultra High
Shorthand	LE/ME	HE	VHE	UHE
Range	0.1–30 MeV	30 MeV–100 GeV	100 GeV–100 TeV	>100 TeV
Typical energy	keV–MeV	MeV–GeV	TeV	PeV–EeV
Environment	Space	Space	Ground-based	Ground-based

Table 1–1: Table of Energy bands as defined by Trevor Weekes [1].

1.5 History of Gamma-Ray Astronomy

The possibility of detecting MeV energy astrophysical photons was predicted in 1958 in an optimistic paper by Philip Morrison [19]. The predicted fluxes of 100 MeV photons were above the sensitivity threshold for spark chambers in balloon-borne detectors, which jump-started the gamma-ray balloon era. However, the gamma-ray balloon experiments were plagued by experimental difficulties which included the high rate of the cosmic ray background. Ultimately, HE gamma-ray astronomy would need satellite detection in order to reduce the background and increase the exposure time [20].

Not long after Morrison's seminal paper, Cocconi produced an equally optimistic prediction for gamma-ray astronomy at VHE energies [21]. The first systematic VHE gamma-ray observations were made in 1960 by a group from the Lebedev Institute [20]. In the following two decades, atmospheric Cherenkov telescopes and air shower arrays were operated around the world, and the first generation of methods for distinguishing gamma rays from comic rays were developed. There was even some evidence for gamma rays coming from the Crab Nebula [22], but without strong statistical significance [2]. In 1968, the first large optical reflector, 10 metres in diameter, was built for the Whipple Observatory located on Mount Hopkins in southern

Arizona. The experiment yielded no immediate results [1] due to the overwhelming cosmic ray background and the absence of methods for distinguishing the background cosmic rays from the gamma ray signal.

In the 1970s, the SAS-2 and COS-B satellite experiments made the first significant HE gamma ray detections between 35 MeV and 5 GeV by detecting diffuse gamma-ray emission coming from the galactic plane as well as isotropic extra galactic radiation [23]. They also showed evidence for 25 gamma-ray point sources, including the Crab and Vela pulsars [24, 25].

The construction of additional detectors followed in rapid succession over the next few years. It was a time of optimism. Despite that, the field went into a time where the earlier detections could not be reproduced. In 1977, Weekes and Turver used the atmospheric Cherenkov imaging technique to distinguish gamma rays from the cosmic ray background [26] for the Whipple experiment. This technique led to a reproducible detection in 1989: The Whipple 10m telescope, which was originally designed to search for TeV point sources, detected the Crab Nebula with 9.0 σ, corresponding to a flux of 1.8×10^{-11} $photons\ cm^2\ s^{-1}$ above 0.7 TeV [27]. In the 1990s, additional solid source detections emerged [2].

1.6 Types of Detectors

The three principal detectors are satellite experiments, atmospheric Cherenkov telescopes, and air shower arrays. Current satellite experiments operate at MeV and GeV energies, atmospheric Cherenkov telescopes operate between 250 GeV and 50 TeV, and air shower arrays operate above 10 TeV [2]. I will discuss some recent experiments beginning with the satellites, but only briefly talk about VERITAS, the

experiment relevant to this thesis. A detailed description of the project is available in the next section.

In 1991, 15 years after the SAS-2 and COS-B satellites, the Compton Gamma-Ray Observatory (CGRO) was launched into orbit. There were four scientific instruments aboard the CGRO. They covered the gamma-ray energy range of 15 keV - 30 GeV [2]. I will list the four experiments, BATSE, OSSE, COMPTEL, and EGRET:

BATSE: The Burst and Transient Source Experiment (BATSE) was designed for detecting gamma ray bursts in order to locate strong transient sources. It was sensitive from 25 keV to 2 MeV [2].

OSSE: The Orientated Scintillation Spectrometer Experiment (OSSE) was composed of four NaI scintillation detectors which could be pointed individually. It detected gamma rays with energies between 50 keV and 10 MeV and was sensitive to diffuse emission from the galactic plane [28].

COMPTEL: The Imaging Compton Telescope (COMPTEL) used the Compton Effect. It had two layers of gamma-ray detectors, and operated from 1 to 30 MeV. COMPTEL detected gamma rays from active galaxies, radioactive supernova remnants, and diffuse gamma rays from giant molecular clouds [2].

EGRET: The Energetic Gamma-Ray Experiment Telescope (EGRET) detected in the highest energy range, from 20 MeV to 30 GeV (Figure 1-1) [2]. EGRET was composed of a spark chamber tracking system followed by an NaI calorimeter. Incident high-energy gamma rays entered the chamber and pair produced. The particle tracks in the spark chambers determined the incoming direction of the gamma ray, and the calorimeter measured its energy [29]. Cosmic rays were vetoed by an

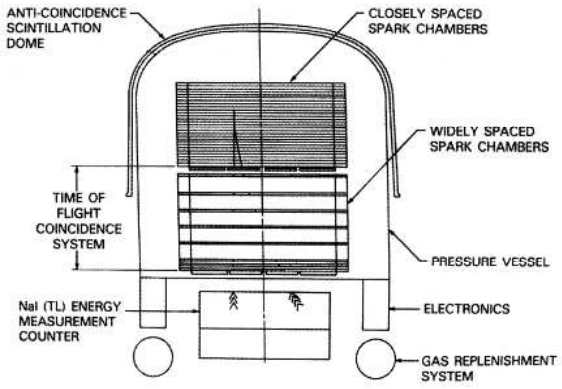

Figure 1–1: A schematic of the EGRET instrument on board the CGRO. Gamma rays interact with spark chambers and produce electron-positron pairs. The trajectories of the electron-positron pairs are tracked through each layer in the spark chamber. Their final energy is measured by an NaI calorimeter. Cosmic rays are rejected by the anti-coincidence shield [2].

anti-coincidence dome. EGRET made detailed observations of high-energy processes associated with diffuse gamma-ray emission, gamma-ray bursts, cosmic rays, pulsars, and blazars [2]. CGRO was de-orbited in 2000.

GLAST is a future high energy gamma-ray mission, developed internationally, and scheduled for launch in early 2008. It consists of two instruments, the Large Area Telescope (LAT) and the GLAST Burst Monitor (GBM). The LAT is composed of a large-area silicon strip tracker, a segmented CsI calorimeter, and an anti-coincidence shield. The LAT will have an order of magnitude improvement in sensitivity compared to EGRET. It will also have a relatively constant effective area up to energies of 300 GeV. Thus many sources detected by GLAST will have a measured energy spectra that overlaps with spectra from ground-based instruments. The GBM uses both NaI and BGO crystals to detect and locate bursts, in a method similar to BATSE on the CGRO. Although its performance will be comparable to BATSE, it

will cover a wider energy range with a smaller collection area. Another experiment, the AGILE mission, will study gamma ray and x-ray sources in the 30MeV - 30 GeV and 10-40 keV energy ranges, respectively [30]. It was developed by Italian institutions and was launched in April 2007 [29].

In the VHE regime, the low gamma-ray flux[2] limits the energy reach of satellite experiments, and ground-based instruments use the Earth's atmosphere as their detection medium, thereby achieving large ($\approx 10^5\ m^2$) effective areas [2]. The Earth's atmosphere is opaque to all gamma rays, however a shower cascade is created by an incoming gamma ray. The particles in the shower travel faster than the speed of light in air, and consequently radiate Cherenkov light which is detected by ground-based Cherenkov detectors. A typical detector consists of an array of photomultiplier tubes (PMTs) located in the focal plane of a large optical reflector. The image of the air shower is used to distinguish gamma rays from the background cosmic rays [4]. The gamma ray signal to cosmic ray background is on the order of 1/1000 at TeV energies [32].

There are some basic differences between gamma ray and hadron shower images. These stem from a physical difference in their shower development due to the smaller transverse momentum of electromagnetic (EM) interactions compared to hadronic interactions. Thus the Cherenkov radiating particles in a gamma-ray

[2] About 6 VHE gamma rays per year would be detected by a 1 m^2 area detector coming from the very bright Crab Nebula, which has an integral flux above 1 TeV of $\approx 2 \times 10^{-7} m^2 s^1$ [31].

shower are on average closer to the direction of the primary. Furthermore, since there are no penetrating hadrons in EM showers the fluctuations in the shower image are less. As a result, gamma-ray images are better defined, making it easier to characterize their arrival direction, and ultimately discriminate against the isotropic background of hadron showers [4]. There are currently four imaging atmospheric Cherenkov detectors worldwide: MAGIC and VERITAS in the Northern hemisphere and HESS and CANGAROO III in the South. HESS' full four-telescope system has been operational since December 2003 and HESS has since produced a wealth of new discoveries [33].

CHAPTER 2
VERITAS Detector

2.1 Basic Design

VERITAS is composed of an array of four identical 12 m diameter imaging atmospheric Cherenkov telescopes located on Mount Hopkins in Southern Arizona (Figure 2–1). VERITAS began making observations in 2003 with a single telescope and continued as successive telescopes were built. The first stereo observations occurred in 2006 and the 2006-2007 season marked the beginning of three telescopes data. The fourth telescope was completed early in 2007 [34].

VERITAS detects gamma rays with energies between about 100 GeV and 50 TeV [35]. Each VERITAS telescope is composed of a light reflector which reflects photons resulting from gamma ray showers onto a light-sensitive camera. The signals from the camera are then digitized by fast electronics, and information from the shower is extracted from the signal. In this chapter, a description of the telescope is presented.

The mechanical design of the telescope is based on the Whipple 10 m telescope. It consists of a welded-steel Optical Support Structure (OSS) placed on a positioner that moves both azimuthally and in altitude. The camera, supported by a quadrapod, is balanced by a counterweight located at the rear of the OSS. The maximum slew speed of the structure is measured to be 0.3 $^{\circ}s^{-1}$ and the pointing accuracy is stable to less than $\pm 0.01^{\circ}$ [3].

Figure 2–1: Left: VERITAS telescope 1 (of four telescopes). The buildings in the foreground are where the electronics and power supplies are located [3]. Right: Close up of VERITAS camera which is composed of 499 Photomultiplier Tubes (Model: XP2970/02) [3].

The reflectors follow a Davies-Cotton design [36] with a 12 m diameter and 12 m focal length. The spherical reflector is composed of 350 hexagonal facets, making up a total area of 110 m^2 [3]. Each mirror facet measures 60 cm across [4] and has a 24 m radius of curvature. The mirrors are made of aluminized and anodized glass with a reflectivity greater than 90% at 320 nm. They are secured to triangular frames on the front of the OSS using 3 adjustment screws that allow for their independent alignment [3].

This Davies-Cotton optical design has several advantages over a large parabolic dish. Firstly, multiple identical spherical mirror facets are cheap to produce and easy to align [4]. Secondly, the mirrors have a smaller off-axis aberration compared to a parabolic reflector. The main disadvantage of this design is that the surface is not isochronous: The reflector introduces a time-spread of about 4ns into the light pulse, which is roughly equal to the inherent width of the shower pulse [4].

The camera is composed of 499 2.86 cm diameter, UV-light sensitive photomultiplier tubes (PMTs). Therefore, the PMTs are sensitive to Cherenkov light, which is peaked in the UV. The quantum efficiency of the PMTs exceeds 20 % at 300 nm. As shown in Figure 2-1, the PMTs are hexagonal-close-packed. The angular pixel spacing is 0.15° with a total field of view of about 3.5° [3]. Light cones are placed in front of the PMTs, which increases the photon collection efficiency by 30%, by redirecting light that would otherwise be lost in between pixels [35]. The gain of the PMTs is set to 2 x 10^5 by adjusting the high voltage (HV) supplied to the tubes by a multichannel modular commercial power supply, which allows each PMT voltage to be programmed separately [3].

After mirror facet alignment, the point spread function (PSF) is measured to be 0.06 ° at the position of Polaris (elevation 21 °) and increases at higher elevations due to the bending of the OSS. The measured PSF is significantly smaller than the 0.15° size of a VERITAS photomultiplier tube. The technique of bias alignment is used to make sure that the smallest PSF occurs when the telescope is in its observing position. In order to accomplish this, the mirrors are purposely misaligned when the telescope in stow position. When the telescope is raised for observing, the structure distorts under its weight such that the mirrors are properly aligned [3].

2.2 Electronics

An outline of the electronics system is illustrated in Figure 2-2. Each PMT signal is amplified by a high-bandwidth pre-amplifier at the PMT. The anode currents are also monitored at the PMTs. The currents typically fall in the range of 0 to 10 microamps, depending on night sky background conditions. The amplified PMT

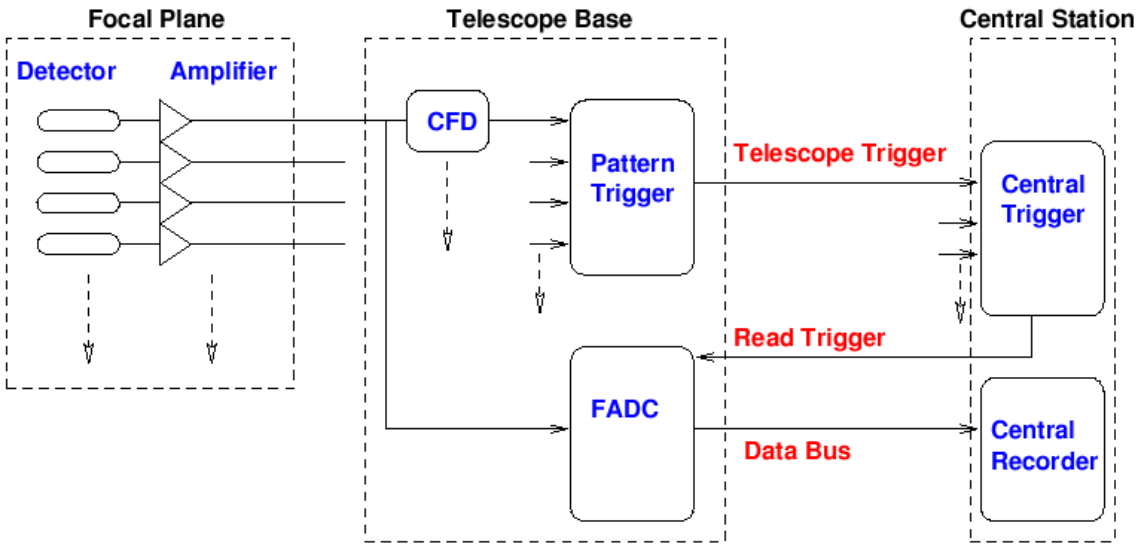

Figure 2–2: Schematic of the VERITAS readout electronics. From left to right, the PMTs (Focal Plane), the telescope base and the central station, which collects data from all four telescopes [4].

signals are sent via 50 m of 75 Ω stranded RG59 cable to the telescope trigger located in the control room and the data acquisition electronics in the electronics trailer [3]. The analog signals are then split, with one of the outputs going to a fast constant-fraction discriminator (CFD) which forms the level 1 trigger [4]. The CFDs are used to produce a trigger time that is independent of the input pulse height, with an output width that is programmable in 12 steps between 4 and 25ns. A copy of the outgoing CFD signal is sent to a topological trigger [37]. This trigger system requires CFD pulses from adjacent pixels to have an overlap greater than 6ns, which substantially reduces the rate of triggers due to random fluctuations of the night sky background. Observations that were made in 2005 with a conservative CFD threshold of 6-7 photoelectrons in a 3-fold adjacent pixel configuration reduced

the cosmic ray trigger rate at high elevation to 150 Hz by lowering the background rate [3].

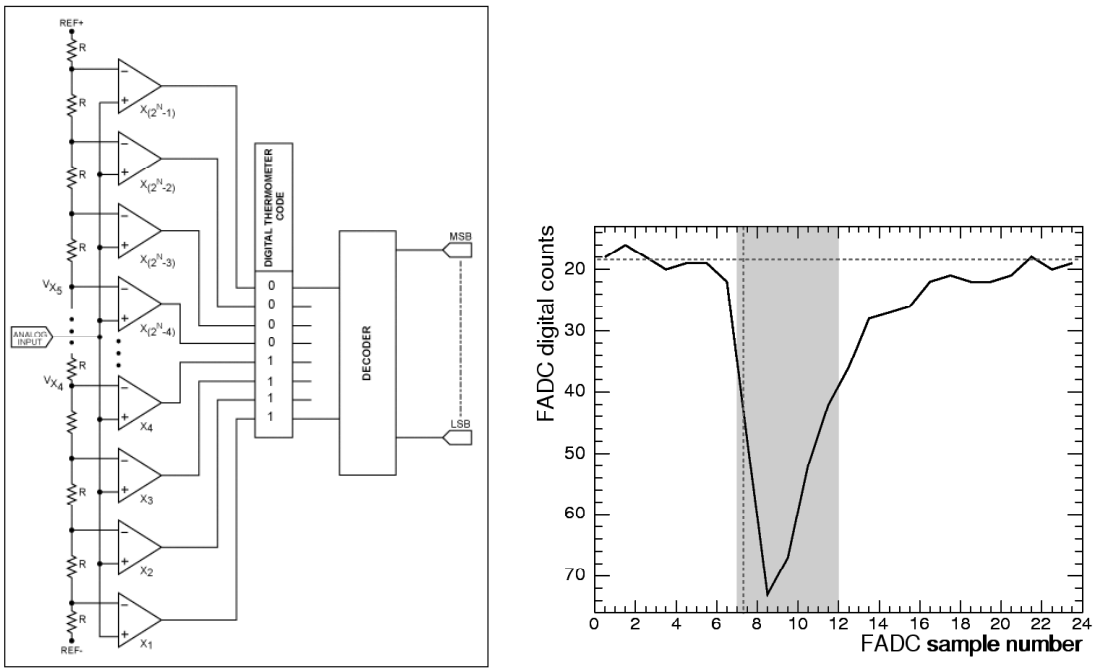

Figure 2–3: Left: A typical FADC block diagram showing how an FADC digitizes an analog input. On the far left, a series of resistors act as voltage dividers. They provide a reference voltage to the comparators, such that the reference voltage to each successive comparator is at least one significant bit greater than the one below it. Each comparator produces a "1" when its analog input voltage is higher than its reference voltage. Otherwise, it outputs a "0" [5]. Right: A typical FADC trace produced by Cherenkov light from a cosmic ray air shower on a single PMT. There are measurements every 2ns connected by a line to guide the eye. The dashed horizontal line is the electronic pedestal level, the dashed vertical line shows the pulse arrival time, and the shaded area indicates a 10ns integration window. The baseline itself has some fluctuations which are due to fluctuations of the night sky background [3].

The second output of the analog signal from each PMT is fed to a 500 MHz flash analog-to-digital converter (FADC) which digitizes the PMT waveform [35]. For a

description on how FADCs work, see Figure 2-3. Each PMT is digitized by an FADC with an 8-bit dynamic range and a memory depth of 32 microseconds. The signal traces follow a high gain path to the FADC, unless the dynamic range is exceeded, in which case an analog switch connects the FADC to a delayed low gain path. The low gain path effectively increases the digital counts from 256 to 1500. A digital count is equivalent to ~ 0.19 photoelectrons at the nominal PMT gain. Figure 2-3 illustrates a typical FADC trace with 2ns sampling.

The telescope trigger signal is sent to the central trigger location where programmable delays are applied to correct for the difference in arrival time of the Cherenkov signal at each telescope [4]. The final signal initiates the readout of the memory of the FADC, where data are recorded.

FADCs are used instead of charge-integrating ADCs because they provide information about the time distribution of the Cherenkov photons, which helps reject the cosmic ray background and improves the accuracy of gamma-ray shower parameter reconstruction. In addition, FADCs allow for active processing of the signal, such as decreasing the charge integration gate, which improves the signal to noise ratio and lowers the effective energy threshold [38].

2.3 Calibration

This thesis is about using different techniques to measure the gain of a photomultiplier tube. In fact, several techniques at VERITAS already exist to measure the PMT gains. However, they are far from redundant. Knowing the gain of the PMTs with great accuracy is essential for being able to determine the amount of Cherenkov light that reaches the camera, and ultimately the energy of the incoming

gamma ray. This section will highlight three gain measurement techniques that are either currently being used at VERITAS or are in the process of being implemented.

Once per night, a laser pulses light uniformly across the entire camera and the response of each PMT is recorded. The relative gain of each PMT is obtained by comparing the integrated charge of the PMT response to the average of all the PMTs. The PMT high voltages are then adjusted to make the response of all PMTs the same, a technique known as flat-fielding (Figure 2–4). The PMT high voltages are adjusted so that the relative PMT gains are within 10% of each other. During the laser runs, the relative time offsets are also recorded. About 95% of the signal channels show a relative time offset of less than $\pm$ 3ns, which is compensated for in the trigger hardware.

The flat-fielding method relies on the assumption that each PMT receives the same amount of light. Therefore, a sophisticated setup is needed to deliver the pulses uniformly across the entire camera of 499 PMTs. To accomplish this, the light is first pulsed by a nitrogen laser, which delivers 4ns wide pulses to a dye module which fluoresces at 400 nm, effectively simulating a Cherenkov wavefront. The light then passes through an optical fibre to a diffuser, positioned about 4 m in front of the camera, which provides uniform illumination [39].

If one could detect a single photoelectron with a PMT, one would be able to directly measure the gain. It would simply be the integrated charge of the PMT signal divided by the charge of the electron. This technique of detecting single photons provides a direct measurement of the PMT gain. However, in order to reduce the light level such that, on average, one photon is detected per light pulse, a special

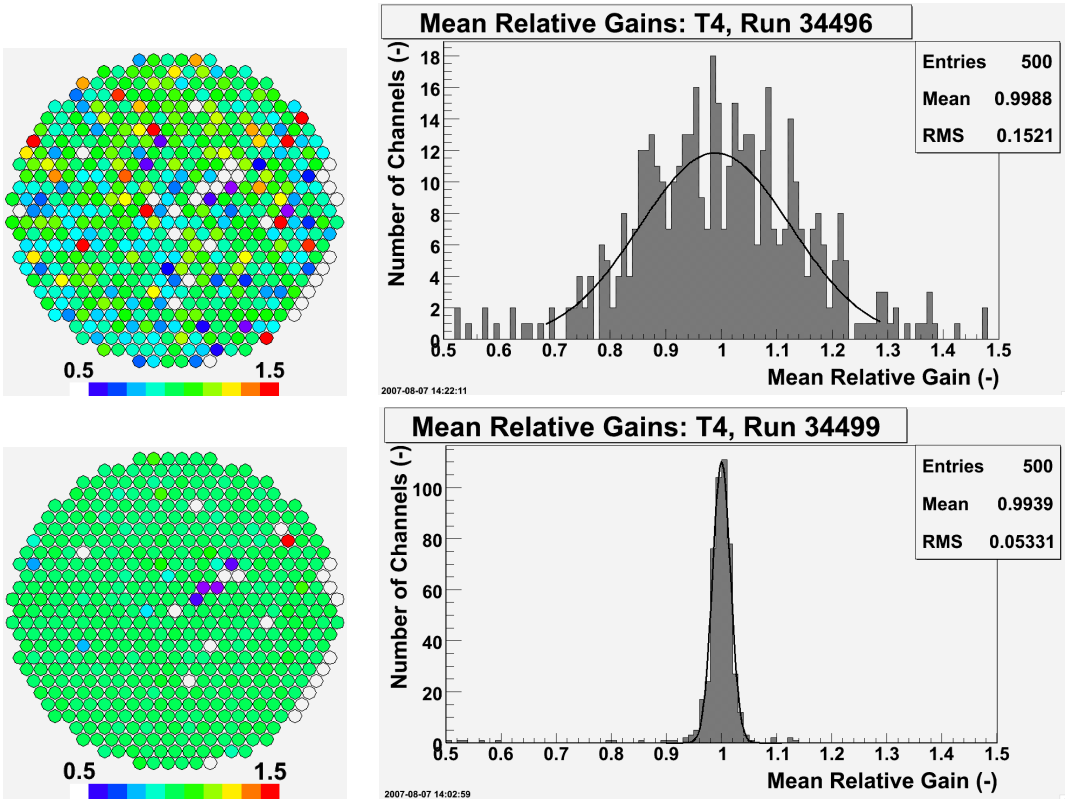

Figure 2–4: The distribution (top) of individual values of the relative gain before flat fielding. The distribution (bottom) of individual values of the relative gain after flat fielding. A laser run of 10^3 events. The information is used to adjust the HV across the PMT (and consequently the gains) such that the pixels respond to light equally.

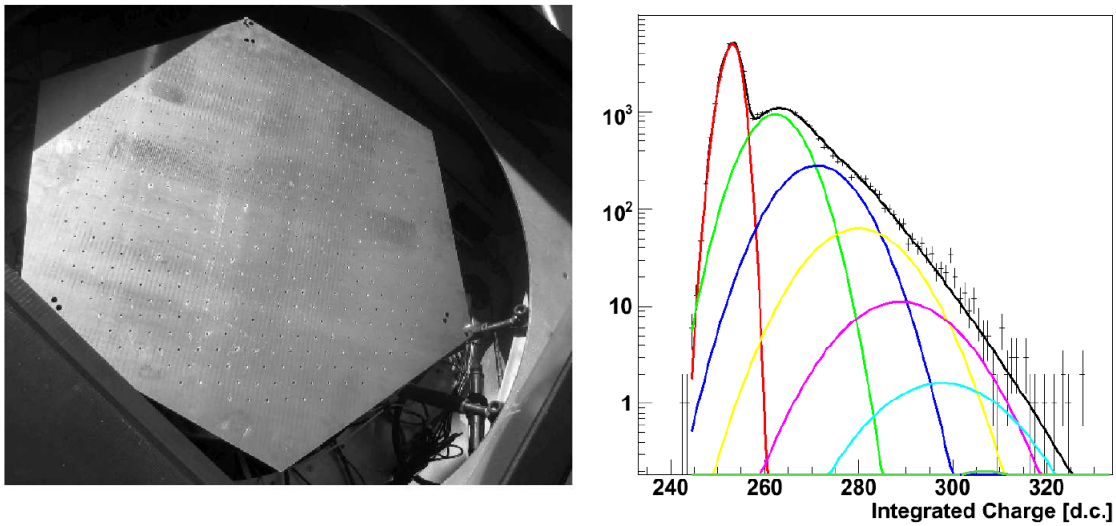

Figure 2–5: Left: Aluminum plate with 3 mm holes in front of each PMT. The plate serves to reduce incoming laser light, such that single photoelectron detection is possible [6]. Right: Fit to the first 5 photoelectron distributions. The left-most peak is the zero photon detection, and the second to left is the single photoelectron peak.

setup is used. Instead of pulsing the laser directly at the camera, an aluminum plate, with 3 mm holes in front of each PMT, is placed in front of the camera (Figure 2–5). When the integrated charge for each pulse is binned in a histogram, one can see the gaussian peaks of the first few photoelectrons. A fit is then used to extract the mean charge of the single photoelectron distribution [6].

Single muon detection offers an alternate method of calibrating the telescope. Muons are easily identified by the characteristic ring image they produce in the camera. Generally, such detections constitute unwanted background, however, it is possible to use their ring image for calibration purposes. Since the distribution of Cherenkov light is a function of the muon's distance of impact from the telescope alone, it is possible to determine the expected amount of Cherenkov light per unit arc length [40]. Summing the output signals of the PMTs across the camera and dividing them by the expected light yield, gives the absolute gain of the camera [40].

In addition to measuring the gain it is also important to measure the night sky background fluctuations and subtract them from the data. Otherwise, one will overestimate the amount of light detected. In order to obtain a measure of the night sky background fluctuations, a pulse generator triggers the data acquisition at 3 Hz in order to generate events without Cherenkov light [39].

CHAPTER 3
Gain

3.1 Photomultiplier Tube

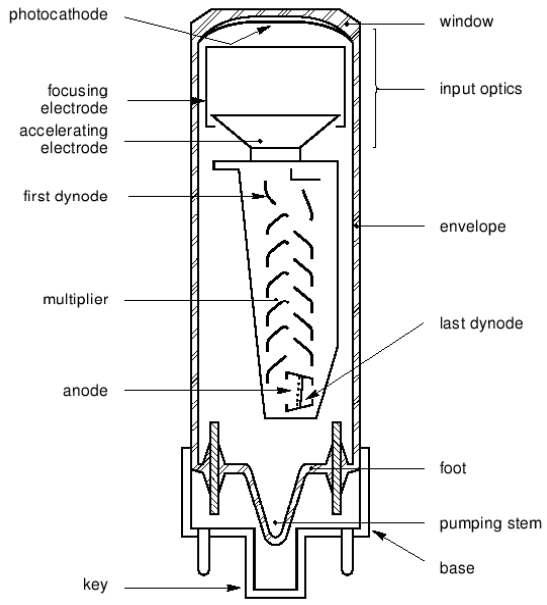

Figure 3–1: Important components of a photomultiplier tube. An incoming photon is converted to an electron at the photocathode. Electron multiplication occurs at every dynode, and the millions of electrons produced are output by the anode [7].

Understanding how a photomultiplier tube (PMT) works is essential to being able to determine its gain. Simply put, a PMT is a device that converts light into an electrical signal (Figure 3–1). The photocathode, usually made of a deposited photoemissive semiconductor, converts the incident light into a stream of electrons

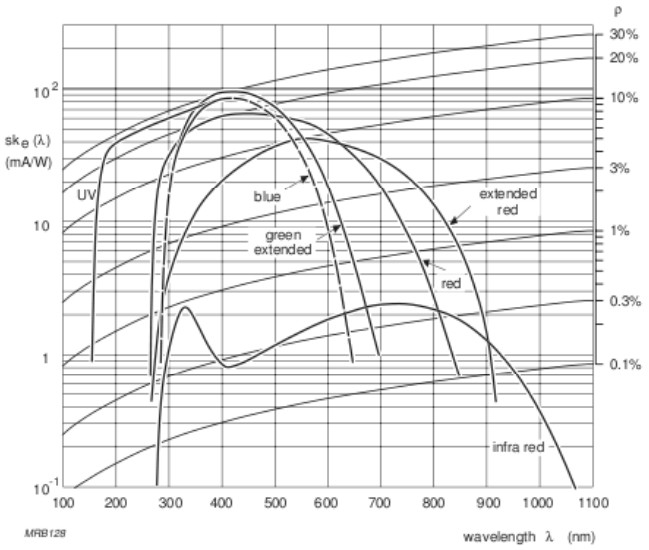

Figure 3–2: The spectral sensitivity for different photocathodes are plotted against wavelength. The curved lines of constant quantum efficiency, ρ, are also shown ($\rho = \frac{S_{k,\lambda} hc}{e\lambda}$) [7].

(See Figure 3–2 for the sensitivities of different photocathodes as a function of wavelength). This occurs via photoemission, where a fraction of the incident photons impart all of their energy to the bonded electrons of the photocathode material, allowing the electrons to escape. The ratio of the number of emitted electrons to the number of incident photons is called the quantum efficiency, and is always less than 1. The resulting electrons, called photoelectrons, are subsequently focused and accelerated towards the first dynode in a series of dynodes which are held at different voltage potentials. Dynodes are usually made of an insulator or semiconductor with an oxidized surface and are arranged such that the electric fields between them cause the electrons emitted by each dynode to strike the next with an energy of a few hundred electron-volts. At each dynode, secondary emission occurs, multiplying the

number of incident electrons. The amount of secondary emission that occurs depends on the potential gradient between the dynodes, which are determined by a voltage divider set up across the terminal of a high voltage supply. The secondary electrons produced by the last dynode are collected at the anode, and constitute the output signal. The overall gain of the PMT is equal to the number of electrons produced at the anode for every photoelectron generated at the photocathode. As such, it is equivalent to the ratio of the anode current to the photocathode current [7].

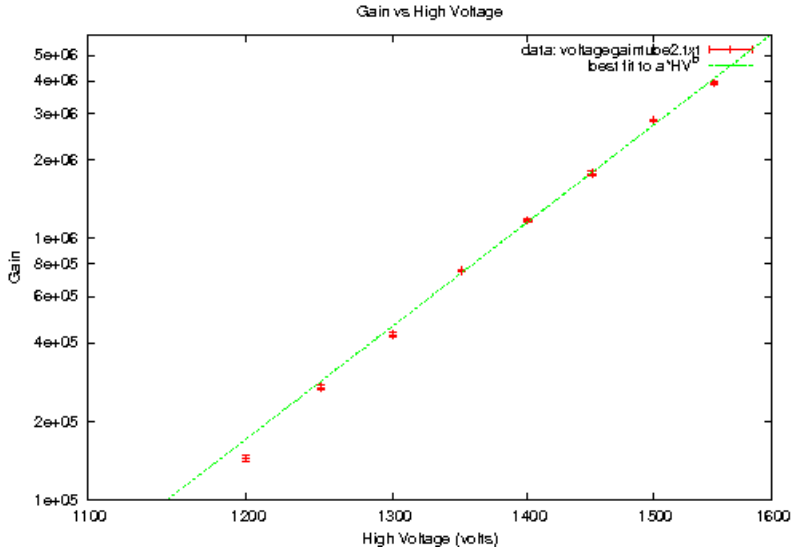

Figure 3–3: Log-log plot of Gain vs High Voltage for a PMT. The equation of the best fit line is $y = 12.36x - 32.82$. The slope of the line, 12.36, corresponds to γ. γ is roughly equal to the number of dynodes in the PMT (XP2212B), which is 12.

The gain of a photomultiplier tube is related to the applied high voltage (HV) via the following equation:

$$Gain = k(HV)^{\gamma} \tag{3.1}$$

where k and γ are constants (Figure 3–3). γ is approximately equal to the number of dynodes in a PMT. The motivation for this equation comes from the geometry of the dynodes. For the majority of the dynodes in a PMT, the voltage difference between successive dynodes is roughly equal, such that the potential difference between successive dynodes is simply the HV supplied to the PMT divided by the number of dynodes. Electrons are accelerated by the voltage potential between dynodes and the amount of energy they impart on the subsequent dynode is proportional to the voltage potential. Therefore, via secondary emission, each dynode multiplies the incoming number of electrons by kHV^1. For a series of γ dynodes, one expects an overall multiplication, or gain, of roughly $k^\gamma HV^\gamma$. The actual derivation is more complex, and as a result γ is not an integer. Furthermore, once k and γ are determined from experiment, equation (3.1) can be used to predict what voltage one would need to apply to a PMT to achieve a given gain.

This thesis explores a new method of measuring the gain of PMTs. As will be described next, the response of a PMT to light can be exploited to measure its gain.

3.2 Measuring the Gain

In chapter 2, several methods of measuring the gain were outlined. I will now go into further detail about one particular method, where a laser is pulsed at the PMTs and the output of the PMTs are used to calculate the gain. I will call this method A, for book-keeping reasons, since it is one of two methods being used. A second method, dubbed method B, will also be explained in detail. Unlike method A, method B is not currently used at the telescope and up to this point, has been motivated [41], but has not been fully developed, tested or implemented at the VERITAS telescope.

Method A provides the gain at different high voltages. Then, the results from method B can be compared with these calculated gains, and the validity of method B can be assessed. This chapter contains the derivations of the two methods.

3.2.1 Method A: σ^2 vs μ

The Poisson distribution is a discrete distribution which describes the probability that a random event will occur in a given interval under the condition that the probability of the event occurring in that interval is small, and the number of trials is large so that the event does indeed occur a few times. For a number of successes, x , with a mean of μ, the probability of x occurring is given by:

$$P(x, \mu) = \frac{\mu^x e^{-\mu}}{x!} \tag{3.2}$$

For Poisson distributions, the mean is equal to the variance ($\mu = \sigma^2$) [42].

Consider the response of a PMT to a pulsed LED at different light levels. The number of photons that hit the PMT in a given time interval (τ) will follow Poisson statistics. Assuming that each photon striking the photocathode of the PMT releases either one or zero photoelectrons, the photoelectron distribution will also be poissonian with mean μ_{pe} and standard deviation σ_{pe}. For large means, Poisson distributions look gaussian (Figure 3–4). Thus, for a large number of incident photons, the initial charge distribution is effectively gaussian with mean μ_i and standard deviation σ_i where $\mu_i = e\mu_{pe}$ and $\sigma_i = e\sigma_{pe}$, and e is the charge of the electron.

The photoelectrons, initially generated at the photocathode, are multiplied in several stages by the dynodes in the PMT. The number of exiting electrons is equal to the number of photoelectrons multiplied by the gain (G) of the PMT. The final

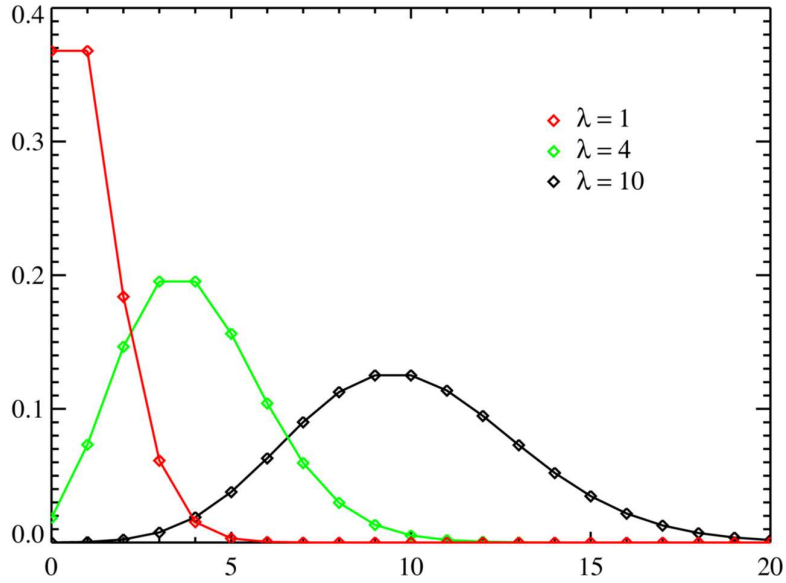

Figure 3–4: Poisson distribution with different means (λ). Note that a Poisson distribution with a mean of 10 already looks gaussian.

charge distribution will be gaussian, with mean, μ_f and standard deviation, σ_f, such that $\mu_f = G\mu_i$ and $\sigma_f = G\sigma_i$. See Figure 3–5 for PMT charge distributions at various light levels and note that they do look gaussian. It is now possible to derive an expression of the gain in terms of the final charge distribution:

$$\mu_i = {\sigma_i}^2, \tag{3.3}$$

$$\mu_i = e{\sigma_{pe}}^2, \tag{3.4}$$

$$\frac{\mu_i}{e} = (\frac{\sigma_i}{e})^2 = \frac{(\frac{\sigma_i}{e})^4}{(\frac{\sigma_i}{e})^2} = \frac{(\frac{\mu_i}{e})^2}{(\frac{\sigma_i}{e})^2} = \frac{(\mu_i)^2}{{\sigma_i}^2}, \tag{3.5}$$

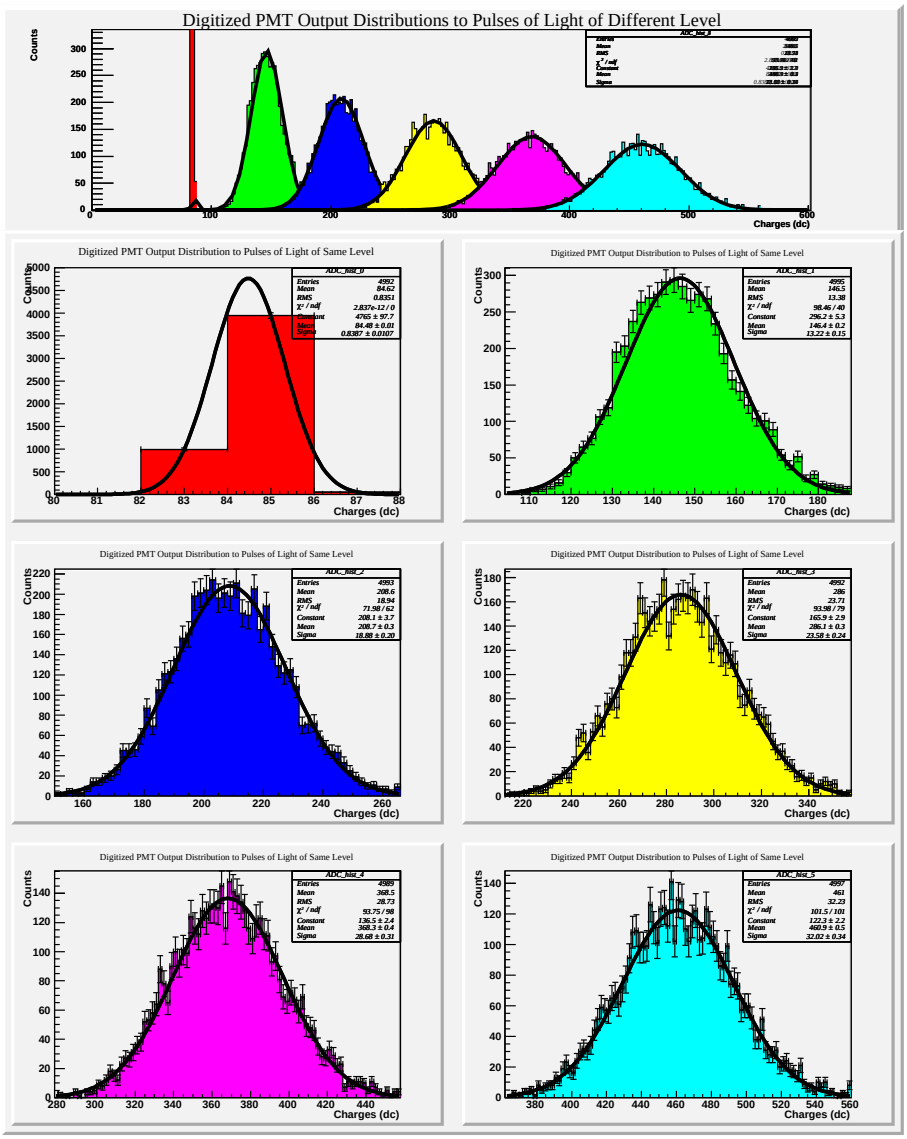

Figure 3–5: Histograms of charge distributions for a PMT exposed to increasing light levels. The first distribution is for a PMT with the light turned off (pedestal). The light level increases from left-right and top-bottom. Every distributions has a mean charge μ and standard deviation σ. Note that as the light level increases, so does μ and σ. Also, note that at the distributions look gaussian.

Substituting equation (3.5) into the definition of the gain, yields:

$$Gain = \frac{\mu_f}{\mu_i} = \frac{\frac{\mu_f}{e}}{\frac{\mu_i}{e}} = \frac{\frac{\mu_f}{e}}{(\frac{\mu_i}{\sigma_i})^2}, \tag{3.6}$$

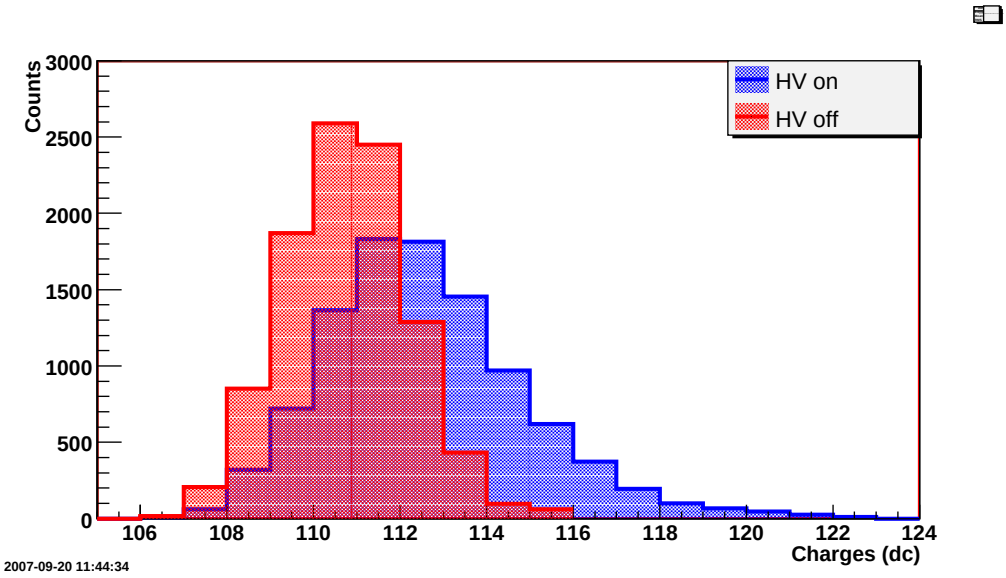

Figure 3–6: Histograms of ADC charges for a PMT at 1650 volts and with the HV turned off. The histogram with the HV off represents the electronic noise of the PMT, and the one with the HV on represents the dark current, an amplified version of the electronic noise.

Up to this point, we have been dealing with a noiseless PMT, but in reality the PMT has a certain level of electronic noise. The average current that a PMT outputs when it is in the dark is called the dark current. A PMT's dark current has a variance, σ_0^2 (Figure 3–6). The average dark current introduces a current offset, however, it does not change the proportionality between σ^2 and μ which is related to the gain. It will merely add an offset, μ_0. The variance of the dark current (σ_0^2) and the variance of the light detected signal (σ^2) are uncorrelated and independent at a given HV. Thus, they will add in quadrature ($\sigma_{total}^2 = \sigma^2 + \sigma_0^2$), such that σ_0^2

merely introduces an offset as well. This leaves the expression for the gain unchanged. Figure 3–7 shows a plot of σ^2 vs μ and the offsets that are introduced.

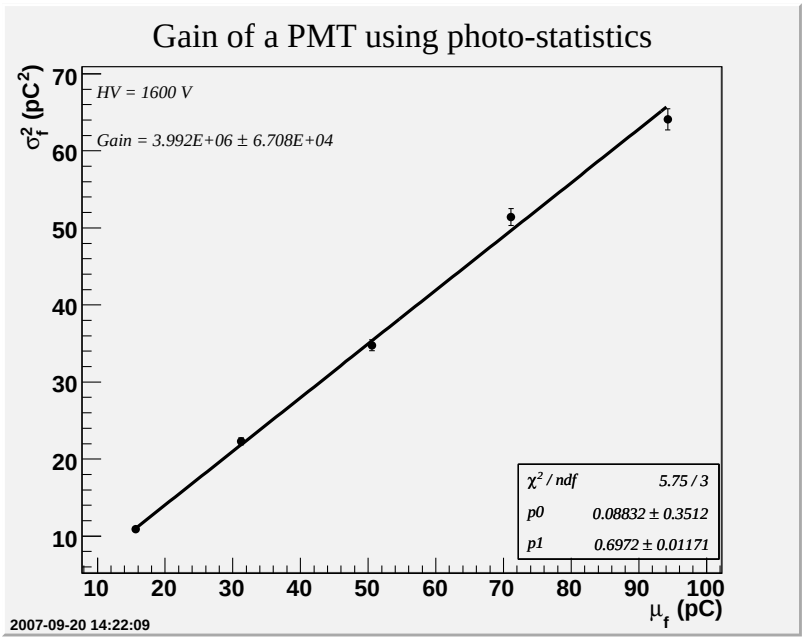

Figure 3–7: σ^2 vs μ for the charge distributions. The gain is proportional to the slope of the line. The y–intercept is due to the upward shift from σ_0^2 and the rightward shift from μ_0. The noise introduces these offsets won't affect the gain, which is proportional to the slope of the line.

We will assume that the gain is linear, meaning that the gain is not affected by the light level. In other words, the PMT multiplies any incoming number of photons by some value G. One obtains:

$$\frac{G\mu_i}{G\sigma_i} = \frac{\mu_f}{\sigma_f}, \tag{3.7}$$

$$Gain = \frac{\frac{\mu_f}{e}}{(\frac{\mu_f}{\sigma_f})^2} = \frac{{\sigma_f}^2}{e\mu_f}, \tag{3.8}$$

In reality, this expression is too simplistic. Electron multiplication occurs in stages, where the number of electrons gets multiplied by a small number at each dynode. Thus, the fluctuations in the secondary emission of each dynode must be taken into account. Such treatment has been statistically done by Lombard and Martin, using the method of generating functions [43]. I will state their main results. Assuming that the electron multiplication process at the dynodes are random, follow Poisson distributions and are independent of each other, one finds:

$$Gain \approx \frac{{\sigma_f}^2}{e\mu_f}\frac{1}{1+\alpha^2} \tag{3.9}$$

$$\alpha = \frac{\sigma_1}{\mu_1 - \mu_0} \tag{3.10}$$

where α is the width parameter, were one to inject single photoelectrons into the dynode chain. This experiment of injecting a single photoelectron would produce an output with average charge, μ_1 and standard deviation, σ_1. Meanwhile, μ_0 is the average charge when no light is present (pedestal).

3.2.2 Method A2: σ^2 vs I

It makes sense to talk about the charge deposited in a PMT signal when using charge-integrating ADCs. ADCs output the charge, making it simple to get the average charge μ_f and its variance. However, this is not the only way to measure the charge, another method involves using the current.

At really low light levels, you can imagine individual pulses resulting from each photon being detected. As you increase the light level, they begin to pile-up on top of each other and the signal begins to look like noise, with an average voltage offset

(Figure 3–8). At this point, one can begin to think of it as a continuous process instead of a discreet one. In this case where the LED is continually on, and the light level is sufficiently high, it makes sense to put the gain in terms of current.

In the case where the LED is constantly on, the current is simply the average voltage divided by R, using Ohm's law. Thus, one can exploit a device that measures the voltage, like an oscilloscope, to get the current. It is also be possible to use an ammeter to measure the current directly. Regardless, of the method of measuring the current, when found, the current relates back to μ_f, the average charge deposited during a time τ. Current by definition, is dQ/dt, where Q is charge, thus:

$$\mu_f = I\tau \tag{3.11}$$

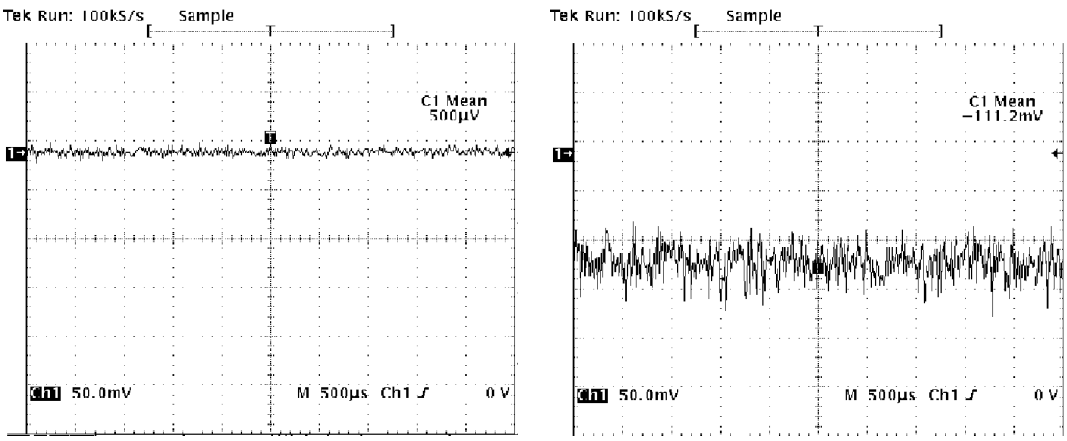

Figure 3–8: Left: A typical PMT trace with the light turned off with an average current of $\sim$ 50 nanoamps, which is referred to as the dark current. Right: A typical PMT trace at 1650 volts with the light turned on at a constant level with an average current of $\sim$ 10 microamps. Note that when the light is turned on, the baseline shifts lower as more pulses add up and the variance increases as well. At this rate it is impossible to distinguish individual photons being detected.

Substituting current for charge, yields yet another expression of the gain:

$$G = \frac{{\sigma_f}^2}{eI\tau}\frac{1}{1+\alpha^2} \tag{3.12}$$

If an FADC or oscilloscope is used to record the signal from a PMT, the output will be in volts. Thus, it makes sense to convert the above equation in terms of voltage variance instead of charge, yielding yet another equation for the gain:

$${\sigma_f}^2 = \frac{{\sigma_{\bar{v}}}^2\tau^2}{(50\Omega)^2}, \tag{3.13}$$

$$G = \frac{{\sigma_{\bar{v}}}^2\tau}{\bar{I}(50\Omega)^2 e}(1+\alpha^2) \tag{3.14}$$

where the input impedance of the FADC or oscilloscope is 50 Ω, ${\sigma_{\bar{v}}}^2$ is the variance of the average voltages, and was introduced using Ohm's law.

3.2.3 Method B: σ^2_{FADC} vs I

The standard deviation of the voltages that make up the trace on the FADC can also be used to calculate the gain. I will show that at low photon rate and low gain, the gain is proportional to the current, and the standard deviation of the FADC trace is a factor in that proportionality.

The following derivation expands on a similar derivation by David Hanna [41]. Assume that the current from the PMT is due to a random occurrence of photoelectrons. Each photoelectron causes a single pulse of average height $< v >$ (volts) confined in a width w (ns). The average rate of photoelectrons is R (Hz) (Figure 3–9). The voltage is either $< v >$ or zero depending on whether the pulse is present,

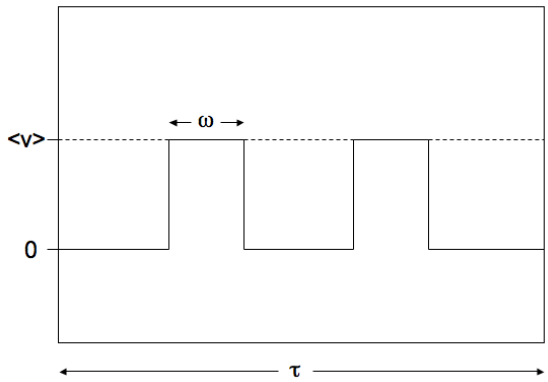

Figure 3–9: Simplified example using positive square pulses with rate R, width w and average height $< v >$ volts, during a time interval τ. Note that the average voltage is simply the fractional time that the pulse is on (Rw) multiplied by the height of the pulse ($< v >$).

thus Rw is the fractional time that you have a pulse. Furthermore, the fractional time of getting a pulse multiplied by $< v >$, gives the average voltage of the trace R$w$$< v >$. Using Ohm's law, the average photocurrent due to the incoming pulses in an FADC is:

$$I = \frac{Rw < v >}{50\Omega} \tag{3.15}$$

This is exactly the average voltage, R$w$$< v >$, divided by the 50 Ω input impedance of the FADC. Since the voltage is either $< v >$ or zero depending on whether the pulse is present. The fractional time of getting a pulse multiplied by its average voltage, yields the average voltage of the trace R$w$$< v >$.

For sufficiently low rates, where overlap is not significant, the FADC variance is described by:

$$\sigma^2 = \frac{1}{N}\sum_{i=1}^{N}(s_i - \bar{s})^2 = \frac{1}{N}\sum_{i=1}^{N} s_i^2 - \bar{s}^2 \tag{3.16}$$

s_i corresponds to the ith sample on the FADC and is in volts and N is the number of points in a given FADC trace (Figure 3–10). $\bar{s}$ is simply the average voltage value of the samples in a given trace and N is the number of points in the trace.

$$\bar{s} = \frac{1}{N}\sum_{i=1}^{N} s_i = Rw < v > \tag{3.17}$$

and $\sum_{i=1}^{N} s_i^2$ is the average of the square of the voltage, $< v >$,

$$\sum_{i=1}^{N} s_i^2 = NRw < v^2 > \tag{3.18}$$

For a square pulse it is evident that $< v^2 >=< v >^2$. But for a more realistic pulse shape, one finds that $< v^2 > \neq < v >^2$. Combining the two previous equations for variance, one gets:

$$\sigma^2 = R < v^2 > w - R^2 < v >^2 w^2 = (50\Omega)I(\frac{< v^2 >}{< v >} + R < v > w) \tag{3.19}$$

For low rates, such that Rw << 1, one gets:

$$\sigma^2 = R < v^2 > w - R^2 < v >^2 w^2 = (50\Omega)I(\frac{< v^2 >}{< v >}) \tag{3.20}$$

The pulse shape of a single photon is described by $v(t) = -At^{3/2}e^{\frac{-t}{\tau}}$ where t is in nanoseconds and τ was on the order of 7ns for a setup that consisted of a burst of

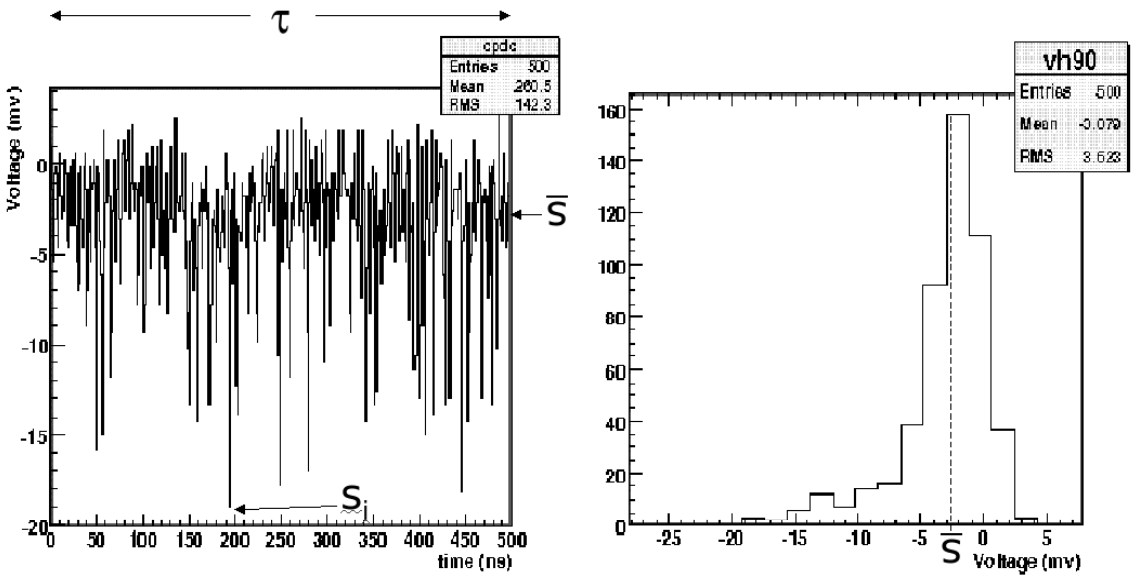

Figure 3–10: Left: An example of a trace resulting from a constant LED source. s_i represents a single voltage reading, while $\bar{s}$ is the average voltage for a given trace. τ represents the duration of the trace. Right: The same voltages put into a histogram. The variance of this distribution is σ^2_{FADC}. Note that the long tail to low voltages is due to the pulse shape spending more time close to zero volts than at large negative values.

laser photons spread out over 4ns (Figure 3–11) [41]. The gain is simply the total charge of a pulse divided by e:

$$G = \frac{\int_0^\infty v(t)dt}{(50\Omega)e}, \tag{3.21}$$

$$G = 22 \times 10^9 A \tag{3.22}$$

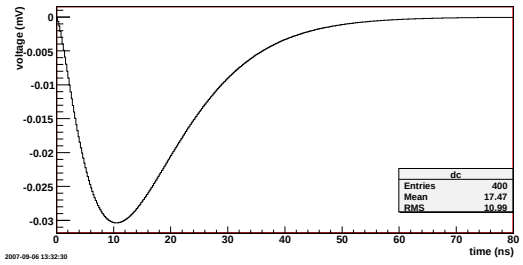

Figure 3–11: A pulse shape of a single photon detected by a PMT, which is described by $v(t) = -At^{3/2}e^{\frac{-t}{7}}$.

Making the substitution $\frac{<v^2>}{<v>} = \beta$, and evaluating the ratio:

$$\beta(w) = \frac{< v^2 >}{< v >} = \frac{\int_0^w v(t)^2 dt}{\int_0^w v(t)dt} \tag{3.23}$$

For large values of w the ratio tends to 5.2A (Figure 3–12). Substituting (3.21) into (3.19) yields the following:

$$\sigma^2 \approx N(< v >^2)Rw = 261.2 \times IA = 1.21 \times 10^{-8} GI, \tag{3.24}$$

$$G = \frac{1}{1.21 \times 10^{-8}} \frac{\sigma^2_{FADC}}{I} \tag{3.25}$$

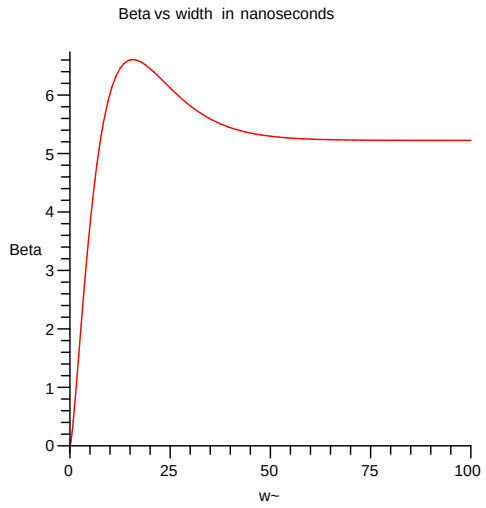

Figure 3–12: Beta plotted as a function of the pulse width. Since nearly all of the individual pulse shape is contained within 50ns, Beta stabilized by 50ns, asymptotically approaching the value 5.2.

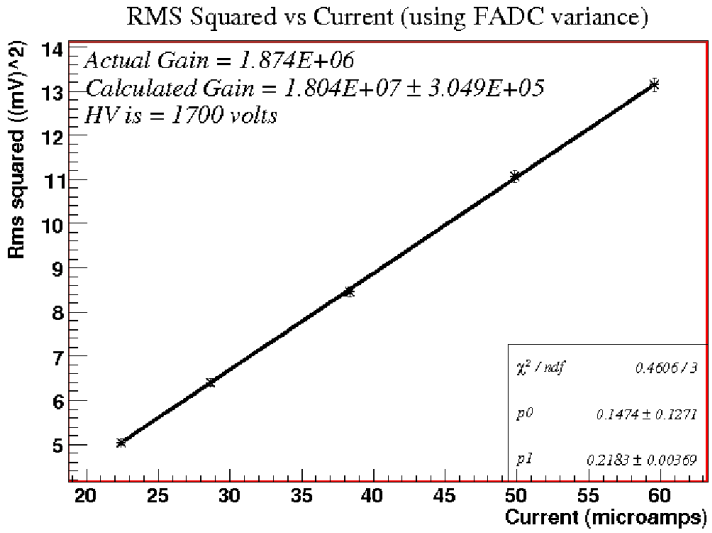

Figure 3–13: The variance, σ^2_{FADC}, plotted against the current. The slope of the line is proportional to the gain, while the variance offset, σ^2_0, is due to PMT noise.

The significance of this equation is that if measurements of σ^2_{FADC} were plotted against current, the slope would yield the gain (Figure 3–13). The purpose of this thesis is to test this technique as a potential method of calculating the gain.

Problems with this method could arise if Rw is not $<< 1$, which should occur at high rates and high gain. This may introduce non-linearity into a σ^2 vs I plot. The effect will be explored later in this thesis. In addition, unlike method A, method B is pulse-shape dependent. Should the response of a PMT to an individual photon have a different pulse shape, the factor relating the gain to the slope will be different. The next step is to test these two methods experimentally. This is described in the following chapter.

CHAPTER 4
Experimental Setup

4.1 Apparatus used in method A: σ^2 vs μ

In this chapter we describe the apparatus used for testing two different methods for calculating the gain. Due to the differences between method A and method B that were described in the previous chapter, a different setup is needed for each of them. We will start by describing the setup used for method A.

A simplified schematic of the experimental setup used in method A is shown in Figure 4-1. The setup had an 8010 pulse generator produce 2 volt, $\sim$ 10ns wide pulses, which were attenuated by a Phillips Model 804 attenuator before flashing a green light emitting diode (LED). The LED was placed roughly 10 cm in front of a PMT in a light-tight wooden box (See Figure 4–2 for a photograph). The LED was connected in series with a 15 ± 5 % Ω resistor series. The PMT response to flashes of different intensity light was recorded.

The PMT high voltage was supplied by a Power Designs 1570 high voltage DC power source. In order to shield the PMT from the earth's magnetic field, a μ metal shield was placed around the PMT [44]. For the most part, the PMTs used in the experiment were of the type XP2282B, and were taken from the recently dismantled STACEE gamma-ray experiment. These PMTs have 8 dynode stages, and a spectral range of 300-650 nm, with a peak sensitivity at 400 nm, which corresponds to violet light [45]. The single photoelectron detection which is described later, made use of

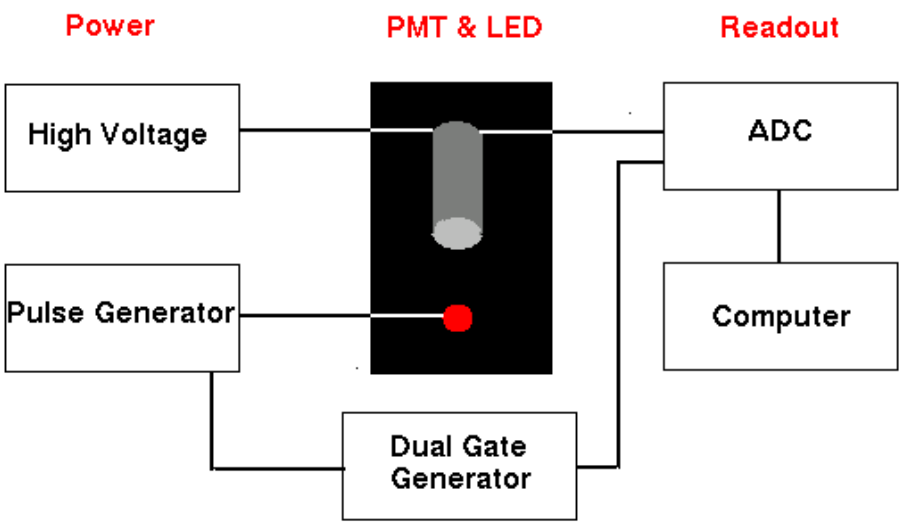

Figure 4–1: A simple schematic of the main components of the experiment used to test method A. The pulse generator supplied $\sim$ 10ns pulses to the LED, whose flashes were detected by a PMT. The PMT signal was then integrated by an ADC within the gate provided by the dual gate generator. The ADC was located in a CAMAC crate, which was connected to a VME crate via a CC32 and a VC32 module. The data was then read out to an on board VME Computer (VMIVME 7750).

Figure 4–2: Left: The PMT and LED were located inside a light sealed box. Right: The inside of the box is shown. The green LED was located at the tip of the small black box facing the PMT and was connected in series with a 15 $\pm$ 5 % Ω resistor. The PMT is encased in a μ metal shield. During the experiment, the box was closed.

the XP2212B, because it was not possible to resolve single photoelectrons with the STACEE PMTs.

A copy of the pulse generator output was sent to a LeCroy 2323A programmable dual gate generator which lengthened the width of the pulse to approximately 70ns. This pulse formed the gate of a LeCroy 2249A Analog-to-Digital Converter (ADC) which sits in a CAMAC crate. See Figure 4–3 for an example of a PMT signal and gate that was sent to the ADC. The length of the gate was minimized in order to reduce background noise, but was made large enough to integrate the entire electrical pulse from the PMT. The ADC integrated the charge deposited by the PMT signal while the gate was on. The charge was subsequently read out by an onboard VME computer (VMIVME 7750) which interfaces with the CAMAC crate

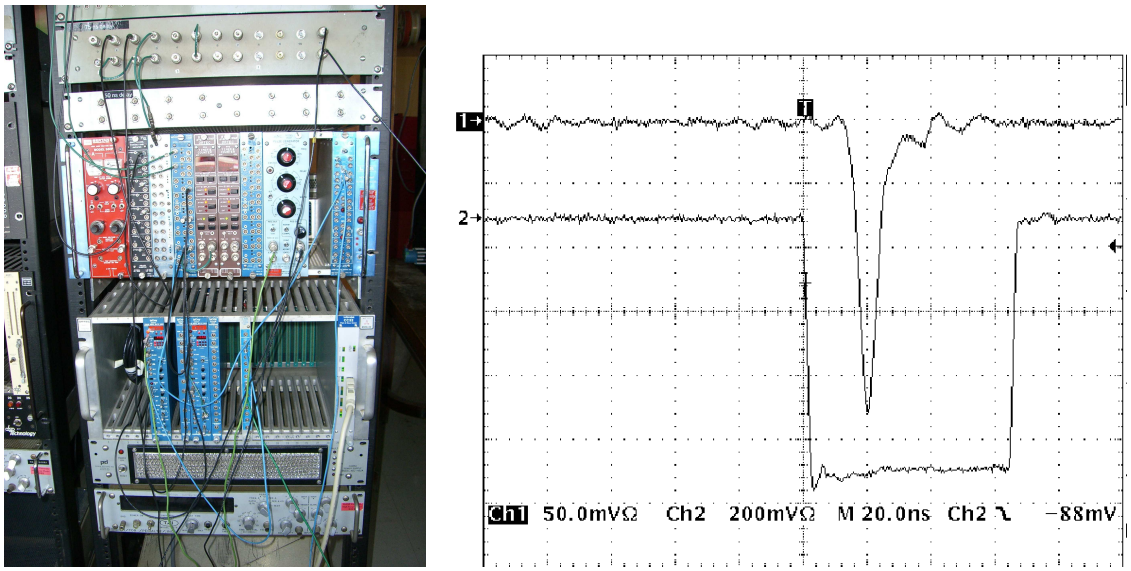

Figure 4–3: Left: The CAMAC equipment used in the experiment, which included a pulse generator, attenuator, programmable dual gate generator and ADC. Right: Typical input to the ADC. The top trace is the response of a PMT to a single 10ns LED pulse while the bottom trace is the gate over which the ADC integrates the pulse.

using a VC32 VME module on the VMEBus connected to a CC32 module on the CAMAC bus. The ADC outputs in digital counts, where one count is equivalent to 0.25 picocoulombs [46].

At each PMT voltage, 5000 ADC values were read in at different light levels and their charge distributions were used to generate a plot of the σ^2 vs μ of the distributions, which lie in a straight line. The slope of that line was then substituted into equation (3.9) to determine the gain. However, that equation also contains the term α, the width parameter of the charge distribution observed, were one to detect single photons. α can be determined directly via single photoelectron detection.

4.1.1 Single Photoelectron Measurements

The setup needed to detect individual photons closely resembles the apparatus used in method A, albeit with some minor alterations. The first addition was the placement of a metal plate with a $\sim$ 2 mm hole in it, in between the PMT and the LED, in order to significantly reduce the light level. Afterwards, the average number of photons detected was approximately one per flash. Another difference was the type of PMT used. For this experiment, the XP2212B was used, since it was able to detect single photoelectrons whereas the STACEE XP2282 tubes could not resolve them. The XP2212B had the potential of having a higher gain without distorting the signal. See Figure 4–5 for an example of the the PMT detecting an individual photon.

The same readout as Method A was used, however longer data sets of 50000 ADC counts were taken at each PMT voltage, producing a charge histogram similar to the ones shown in Figure 4–4. This resulting charge distribution was then fit

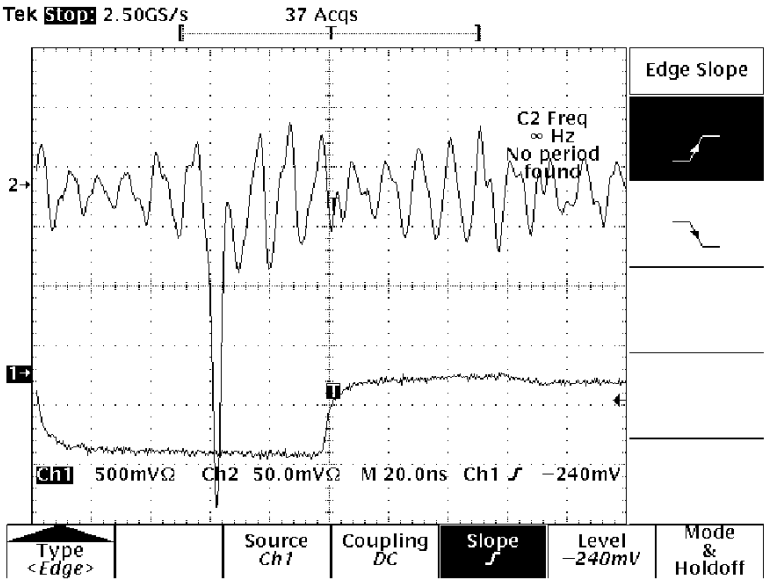

Figure 4–4: The signal of a single photoelectron as seen by the ADC (top trace). The ADC will integrate this signal while the gate (bottom trace) is on, and output the charge in ADC units.

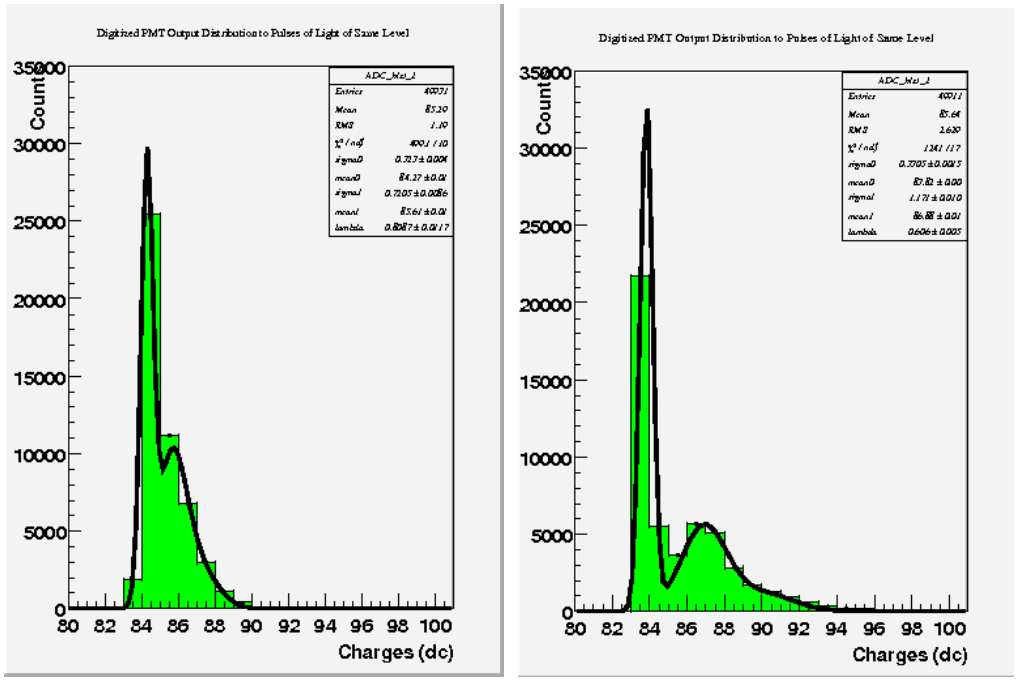

Figure 4–5: Left: ADC output at 1500 volts with fits for the first three photoelectron peaks. Right: ADC output at 1600 volts. Note that the first photoelectron peak moves away from the pedestal at higher PMT voltage.

to the expected distribution for the first few photoelectrons. The expected distribution forces the number of N photoelectron events observed to obey a poissonian probability function. Furthermore, the distance separating the peaks of successive photoelectrons is equal. The multiple photoelectron fit identifies the width and the location of the single photoelectron peak, so that α can be calculated.

4.2 Apparatus used in Method B: σ^2_{FADC} vs I

The apparatus used in method B is illustrated in 4–6. Method B differed from method A by having a constant LED light source, as opposed to a pulsing one. In order to generate a constant LED light source, a DC power supply was connected to the LED. In addition, instead of calculating the variance of the charge distributions, the variance of the samples of individual traces were calculated. As a result, the ADC used in method A was replaced by a digital oscilloscope (Tektronix TDS 620B), which functioned much like an FADC with a very long window (See Figure 4–7 for a photograph of the oscilloscope used). In total, 3000 traces were recorded at a given gain and light level. Each trace had 500 samples and was 1000ns long. An example of a typical oscilloscope trace is provided in Figure 4–7.

The oscilloscope was connected to a computer via GPIB interface. The oscilloscope triggered automatically, and one trace was collected by the computer every few seconds, which was the fastest speed possible.

In addition to the the experiments that have been described, a simulation program was also written to test both method A and method B. First, a single photon pulse with the equation $v(t) = At^{3/2}e^{\frac{-t}{\tau}}$, with $\tau = 7ns$, was simulated. This equation represents the expected response one would observe on an oscilloscope in DC mode,

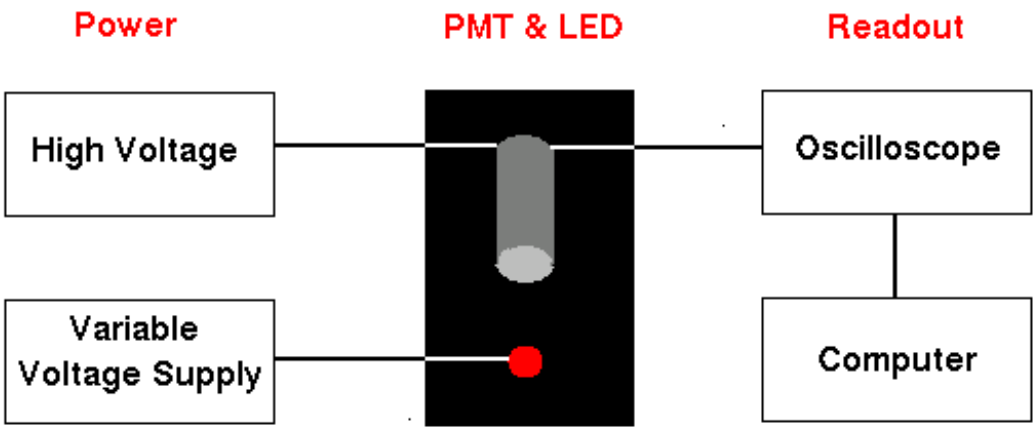

Figure 4–6: A simple schematic of the main components of the experiment used to test method B. A DC power supply provided a constant voltage to an LED which emitted low intensity light. The PMT signal was sent to an oscilloscope, which was then read out by a computer via GPIB interface.

with 50 Ω impedance, if a PMT detected a single photon. Then, by overlapping randomly occurring pulses, traces with different currents were simulated, in a method that will be described in some more detail in the simulations chapter.

This experimental setup has now been described in some detail. However, there were some components of the experiment that needed to be calibrated prior to data collection, and that is the focus of the next two sections.

4.3 Optimizing the read-in rate

This section describes how the optimum read-in rate of the ADC was determined. The setup used in method A involved pulsing an LED in front of a PMT whose output was integrated by an ADC before being read into a computer. Although it

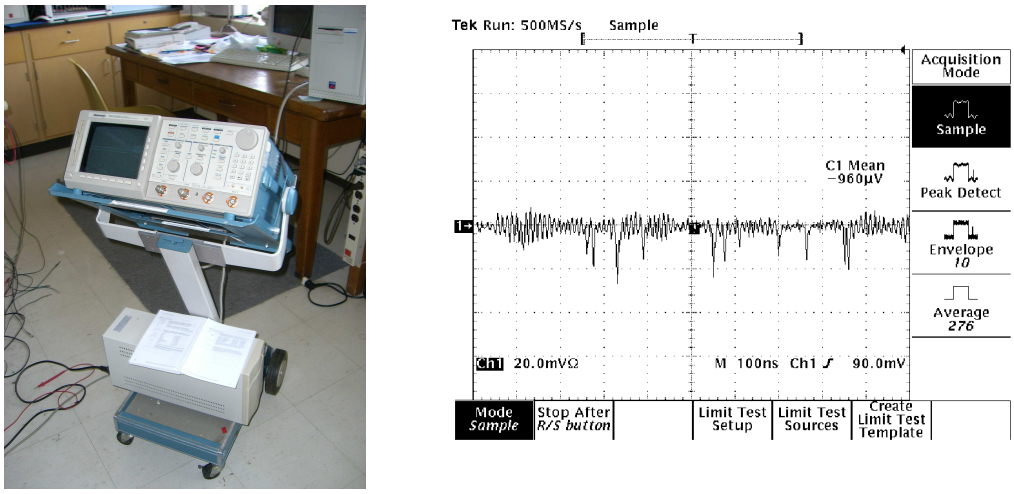

Figure 4–7: Left: The Tektronix oscilloscope used in the experiment. Right: A typical trace on the oscilloscope of a PMT (XP2212B) illuminated by an LED with a constant light level. The trace is made up of 500 points and is 1000ns long. The current of the signal in this particular trace is approximately 20 microamps and the HV applied to the PMT is 1650 volts. The large spikes corresponds to the detection of individual photons. These occur at random times throughout the trace as is expected. Furthermore, note that the trace also has an RF noise component.

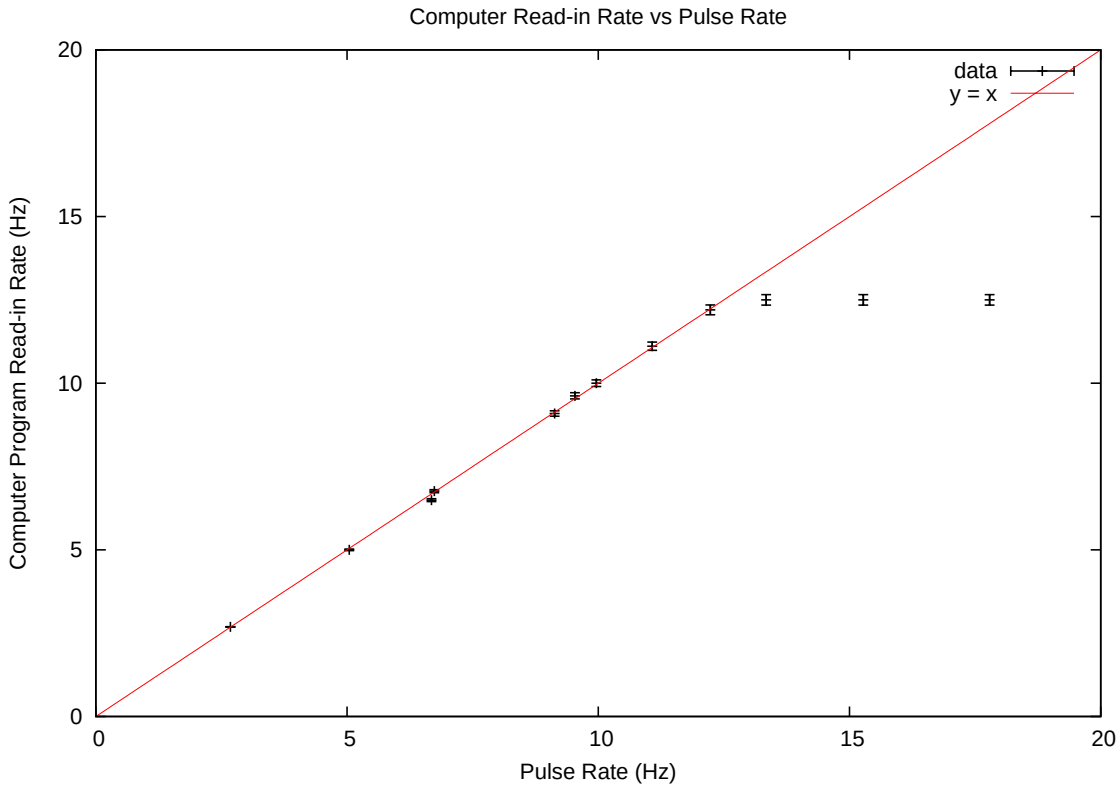

Figure 4–8: The rate that the computer reads in values from the ADC plotted against the pulse rate of the LED. At about 12 Hz, the read-in rate reaches a plateau, as the ADC cannot not read at speeds faster than 12 Hz.

is possible to pulse the LED at very high speeds, the relatively slower speed of the CAMAC technology of the ADC limits the speed of the experiment. Determining the maximum read-in rate of the ADC is a worthwhile undertaking because operating at the maximum read-in rate of the ADC maximizes time efficiency and maximizes the time that the PMT can stabilize between pulses.

A simple experiment was executed in order to determine the read-in rate of the ADC: the pulse rate of the LED was recorded for a range of rates and was compared at each rate with the actual read-in rate of the ADC. Figure 4–8 shows the maximum read-in rate was $\sim$ 12 Hz. Consequently, the LED was pulsed at a value slightly less than the 12 Hz cut-off, which was chosen to be 10 Hz.

4.4 Investigating the PMT warm-up time

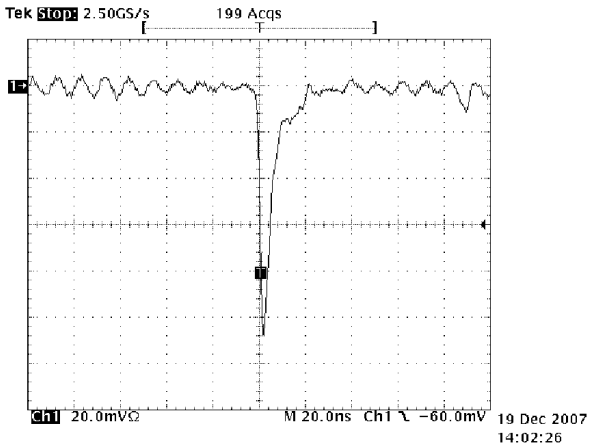

Figure 4–9: Typical PMT response to a flash of light detected from a ^{241}Am source embedded inside a small piece of plastic scintillator. The PMT is at 2500 volts.

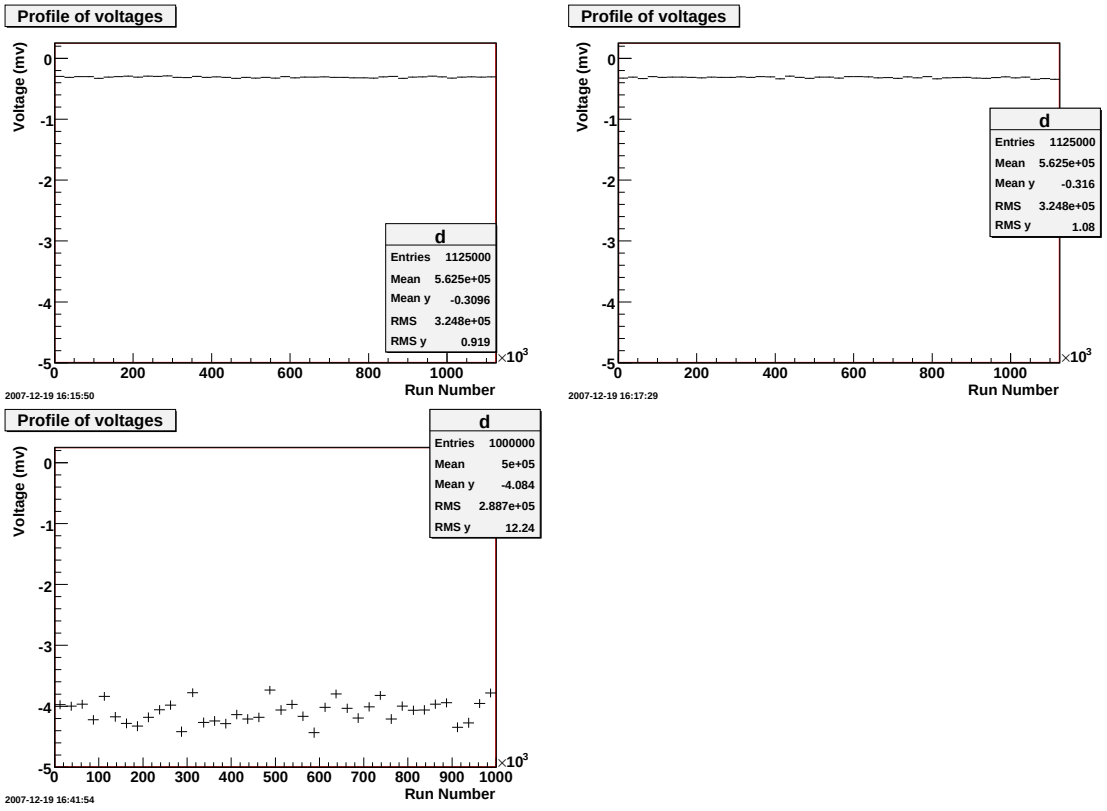

Figure 4–10: The average amplitude of the PMT pulse due to light from alpha decay for three PMTs at 2500 volts as a function of run number. The data set was taken after the HV was first turned on. Each point represents the average of 50 traces read in with the oscilloscope and the data points are separated by a 100 s delay. Each plot is of 2 - 3 hour duration. No significant trend was observed, suggesting that the PMTs do not need time to warm up.

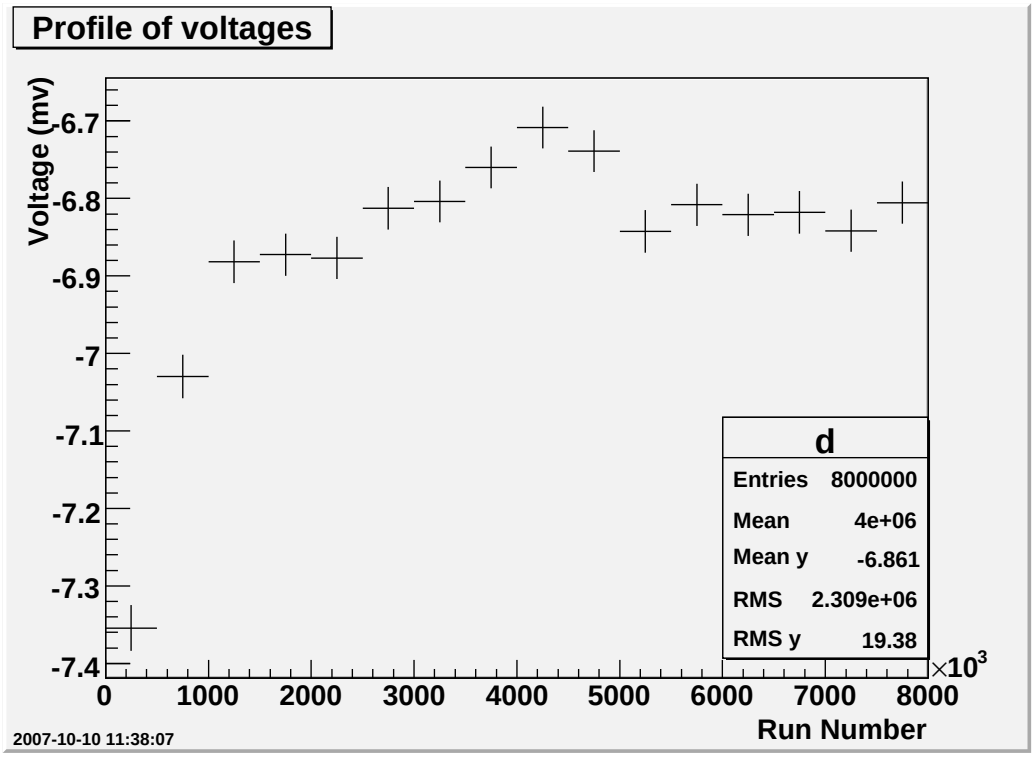

Figure 4–11: Amplitude of the PMT signal vs time. Both the PMT and the LED were turned on and the average amplitude of the PMT signal was read out. This is a plot of the amplitude of the PMT signal as a function of run number, such that each point on the graph corresponds to approximately 15 minutes, or 1000 traces. Note that after a few hours, the light level stopped decreasing and the system stabilized. Also note the suppressed zero.

When a PMT's HV is first turned on, it is possible that it takes a certain amount of time for the gain of the PMT to stabilize. The existence of this so-called warm-up time was investigated by a simple procedure that involved reading in the PMT output directly after the PMT's HV was turned on. Meanwhile, the PMT was being exposed to a constant light source.

The constant light source used was a ^{241}Am source embedded inside a small piece of plastic scintillator. Via alpha-decay, the ^{241}Am source released alpha particles that excited the surrounding scintillator so that it produced flashes of light (Figure 4–9). On average, the amount of light indirectly produced by the alpha decay process is constant.

Three XP2282B PMTs were tested with the scintillator placed directly on the photocathode of the PMT. The signal from each PMT was read out for $\sim$ 2 hours after the PMT's HV was turned on. Since the light source was constant, any changes in the average size of the signal detected could be attributed to a change in the PMT gain. Ultimately, the PMT gain did not appear to change over time, thus no warm up time was observed (Figure 4–10).

Although the PMT did not show evidence for a warm-up time, the LED did (Figure 4–11). It is interesting to note that in the case where the LED is turned on for the first time after a being off for several days, it takes time for the light level to stabilize. Before reaching equilibrium, the LED light intensity decreases as a function of time.

CHAPTER 5
Simulation Results

Both methods A and B for measuring the gain were already motivated using a simple theory. This theory will now be compared to simulations. This section aims to describe these simulations used in detail as well as well as the important results. In this section, method A2, which uses substitutes the charge for current (See Equation 3.12), will be used. This expression makes more sense for constant light levels as opposed to single flashes of light.

A program was written using ROOT [47] and C++. First, a single photon pulse with the equation $v(t) = At^{3/2}e^{\frac{-t}{\tau}}$, with $\tau = 7$ns, was simulated (Figure 3–11). This equation represents the response one would expect to observe on an oscilloscope in DC mode, with 50 Ω impedance, were a PMT to detect a single photon. The input gain was calculated by integrating the pulse. The program then proceeded by adding multiple pulses in order to make up a trace, such that the arrival of the pulses was random. Pulses that reached the end of the trace were overlapped at the beginning. The simulations were executed under two conditions, with $\alpha = 0$, and $\alpha = 0.25$. As was previously defined in Chapter 3, α is equal to $\frac{\sigma_1}{\mu_1 - \mu_0}$. $\alpha = 0$ means that the single photoelectron peak has zero width, and $\alpha = 0.25$ means that the width of the single phototelectron peak is equal to a quarter of its pedestal-subtracted mean.

5.1 $\alpha = 0$

α was set equal to 0 by making every photoelectron pulse equal in size. The data generated by the simulation program are shown in Figure 5–1. In total, 200 traces were simulated at each of 12 different light levels, with the current ranging from 0 to 100 microamps. Calculating the value of the input gain amounted to integrating the pulse shape and dividing it by e. The amplitude of the pulses were fixed such that the input gain was 2.153×10^6.

Using the total set of 2400 (200 traces $\times$ 12 light levels) simulated traces, both methods A2 and B were tested (Figure 5–1). Using equation (3.12), method A2 resulted in a gain of $2.12 \pm 0.06 \times 10^6$ (Figure 5–2). The input gain of 2.153×10^6 lies within error of this measurement, thus the results for method A2 are consistent. Using equation (3.25), method B gave a more accurate and more precise measurement of the gain, $2.161 \pm 0.002 \times 10^6$. However, the input gain does not lie within the error but is close to it. The errors are produced from the straight line fit. Based on this set of simulations, both methods A2 and B should be capable of predicting the gain to within a few percent.

5.2 $\alpha = 0.25$

The same simulations were repeated, however, with non-uniform pulses. The scale height of each simulated pulse was assigned a random value, such that 68% of the scale heights fell within 25% of the average height. Thus, α, which is equal to $\frac{\sigma_1}{\mu_1 - \mu_0}$ as was described in Chapter 3, is 0.25. For these simulations, method A calculated a gain of 2.18 ± 0.04 was obtained while method B resulted in a gain of 2.163 ± 0.002 (Figure 5–3). Similar to the previous simulation where $\alpha = 0$, the

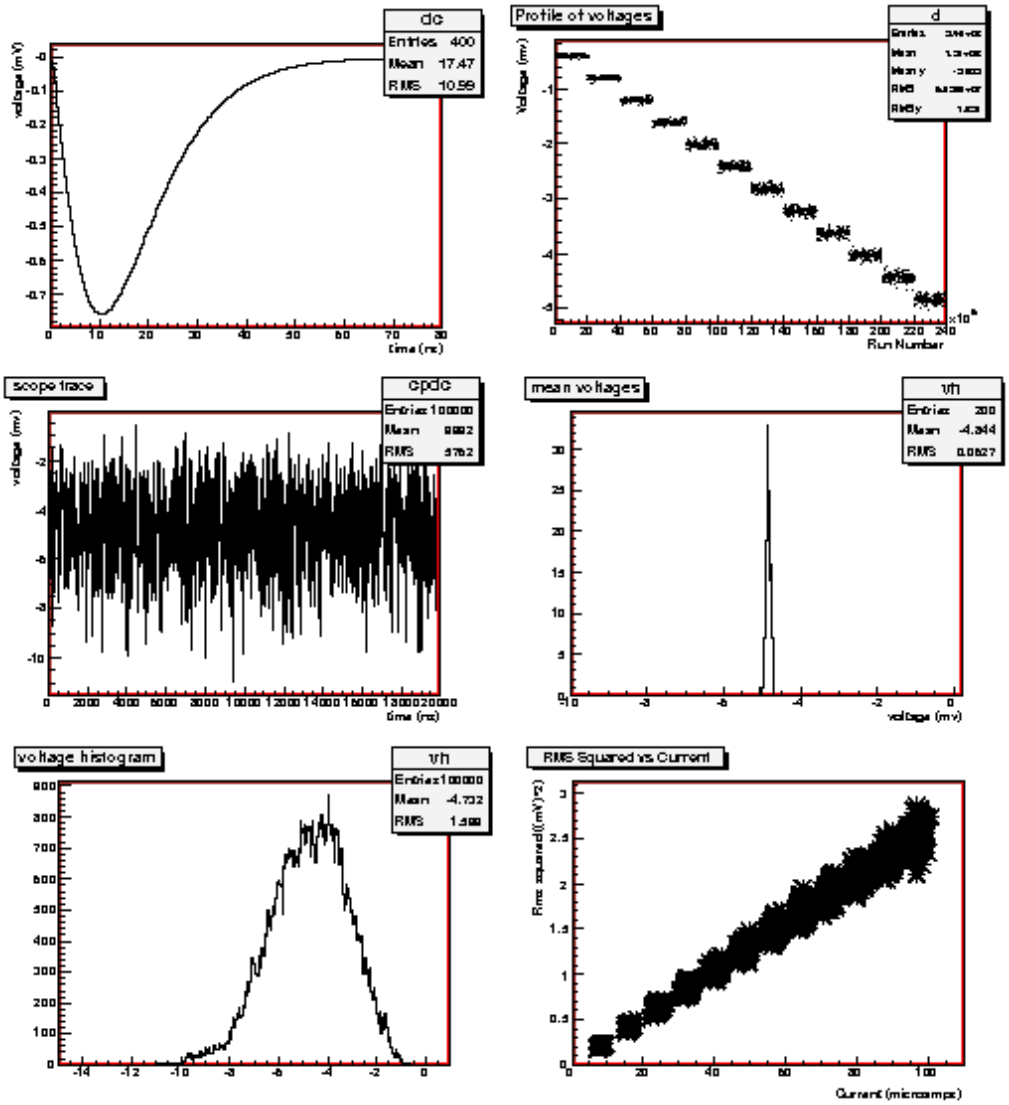

Figure 5–1: Simulated data at 12 light levels (1) the response of a PMT to an individual photon as seen on an oscilloscope (2) the amplitude profile (3) a simulated trace at 100 microamps (4) a histogram of the mean voltages of all 100 microamp traces (5) a histogram of a sample trace at 100 microamps (6) σ^2_{FADC} vs I

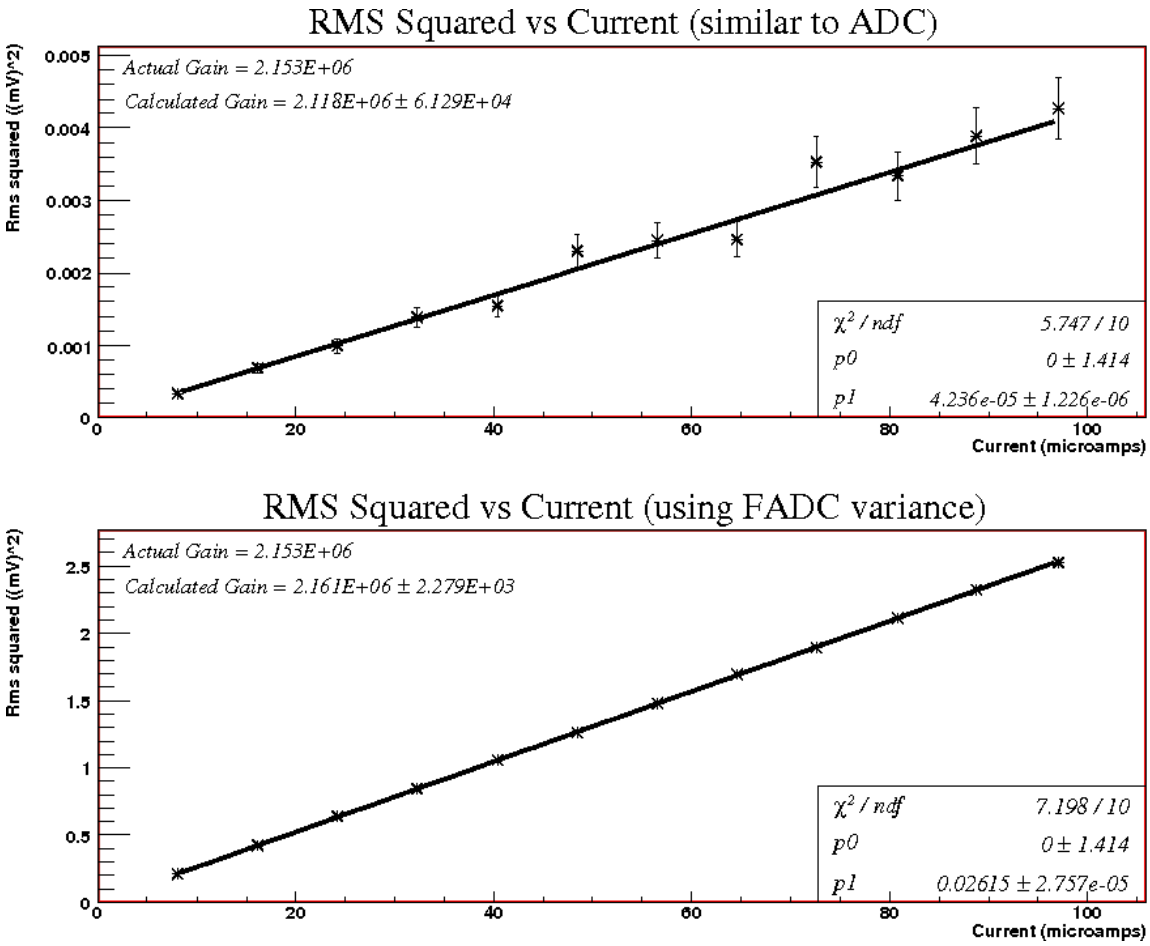

Figure 5–2: Top: σ^2 vs I with error and the best line fit forced through the origin. The slope is used to calculate the gain of $2.12 \pm 0.06 \times 10^6$ using method A. The actual gain of 2.153×10^6 lies within error of this value. Bottom: σ^2_{FADC} vs I with error and the best line fit forced through the origin. The slope is used to calculate a gain of $2.161 \pm -.002 \times 10^6$ using method B. The actual gain is close to this value but not within error.

actual gain lies within the errors of method A, and close to method B. Again, this supports that both methods should be capable of predicting the gain to within a few percent.

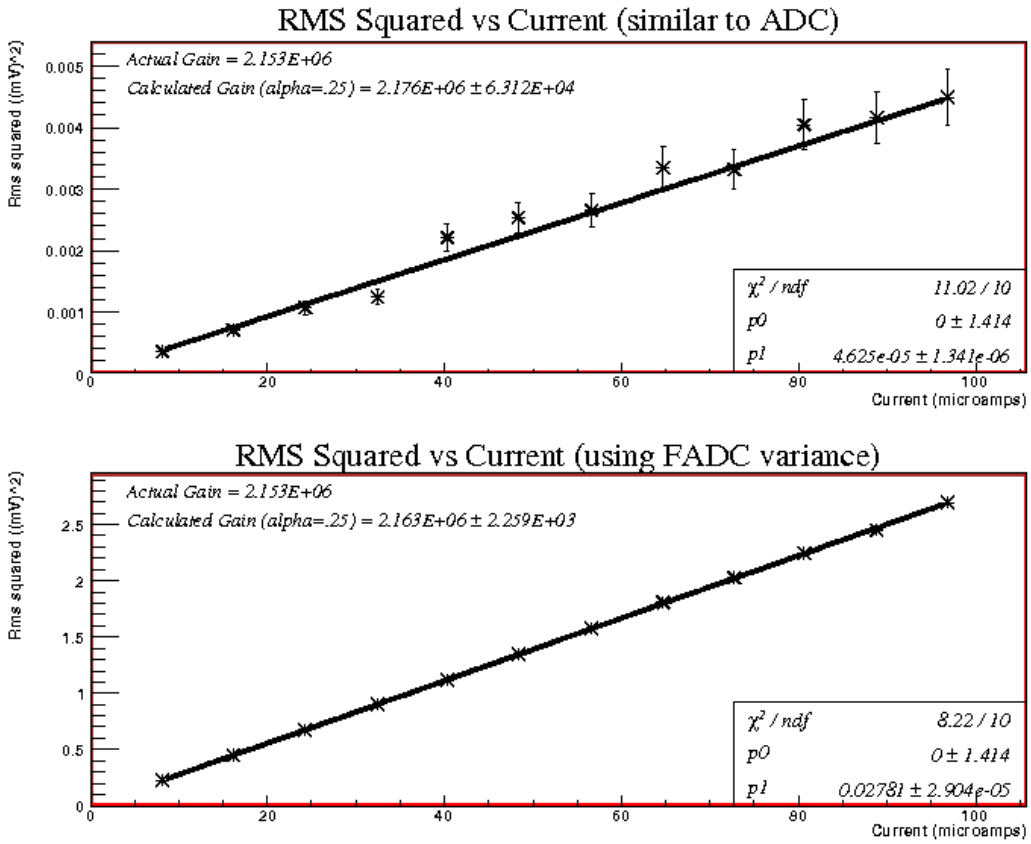

Figure 5–3: Top: σ^2 vs I with error and the best line fit forced through the origin. The slope is used to calculate the gain using method A, and gives a value of $2.12 \pm 0.06 \times 10^6$, within error of the actual gain of 2.153×10^6. Bottom: σ^2_{FADC} vs I with error and the best line fit forced through the origin. The gain is calculated using method B and the slope of the line and yields a value of $2.163 \pm 0.002 \times 10^6$.

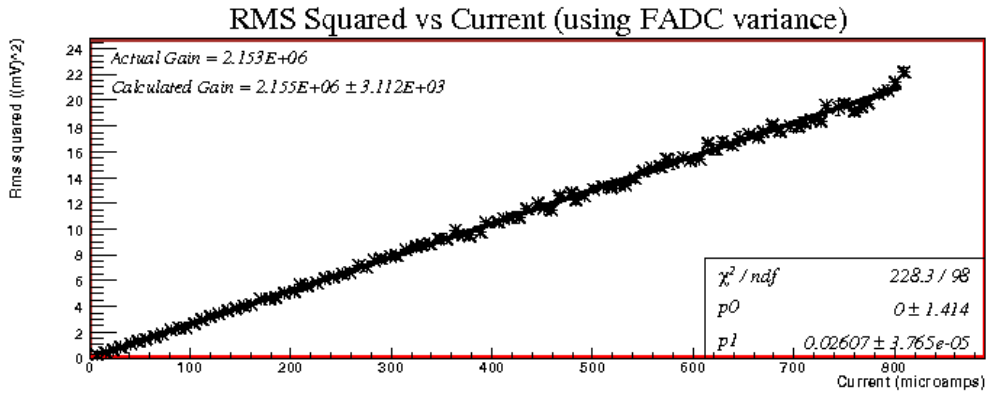

Figure 5–4: σ^2 vs I with error and the best line fit forced through the origin for currents up to 800 microamps. The trend remains linear for the entire range.

5.3 Deviations from Linearity

A low limit approximation for Rw was used in the derivation of the gain in method B, requiring $Rw << 1$. Recall that R is the rate of the incoming pulses and w is the width of a pulse. As long as this approximation is valid, the gain should be proportional to σ^2_{FADC}/I, otherwise some higher order terms result. Furthermore, R increases with current. In order to investigate the potentially non-linear effects, simulations were done at the gain of 2.153×10^6, and the currents were increased to up to 800 microamps, which is well-beyond the regime that a PMT should be operating in (Figure 5–4). This simulated a high-rate environment. However, even at high current, the relationship between σ^2_{FADC} and current remained linear. This justifies the use of the low rate approximation.

CHAPTER 6
Results

This chapter focuses on the gains measured using different methods, one of which is known to function and the other which is being tested. Since method A relies on measurements of the width and mean of the single photoelectron peak, the single photoelectron results will be presented first.

6.1 Single Photoelectron Detection

It was found that it was not possible to detect individual photons using the XP2282B PMTs since the single photoelectron peak was located too close to the pedestal to be resolved (Figure 6–1). A simple calculation shows that at gains typical for this type of PMT ($\sim 6 \times 10^5$), the single photoelectron peak would lie less than one ADC count away from the pedestal. The PMT gain could be further increased, however single photon resolution depends more on the dynode material than the gain (especially the material of the first dynodes). Therefore, increasing the gain would still not resolve a single photon. The inability to distinguish the photoelectron peak suggests that α is large. Were α to be small, one would observe the single photoelectron peak to be well separated from the pedestal.

The procedure for the single photoelectron detection method was carried out with an XP2212B PMT instead. This particular PMT is able to resolve the single photoelectron peak. Since the α values for one PMT is not the same as a different type of PMT, the results from this experiment cannot be combined with the results

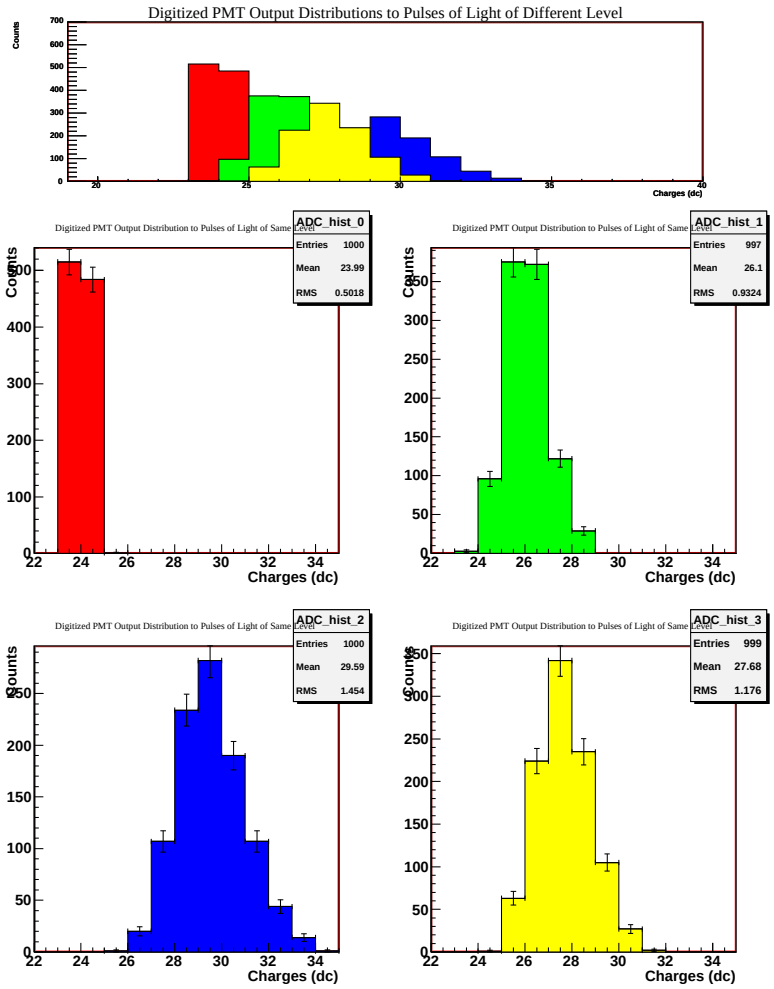

Figure 6–1: ADC output at 2500 volts using a XP2282B PMT for the pedestal (top left) and three low light levels. The light level is slowly increased from zero but the single photoelectron peak lies too close to the pedestal to be resolved.

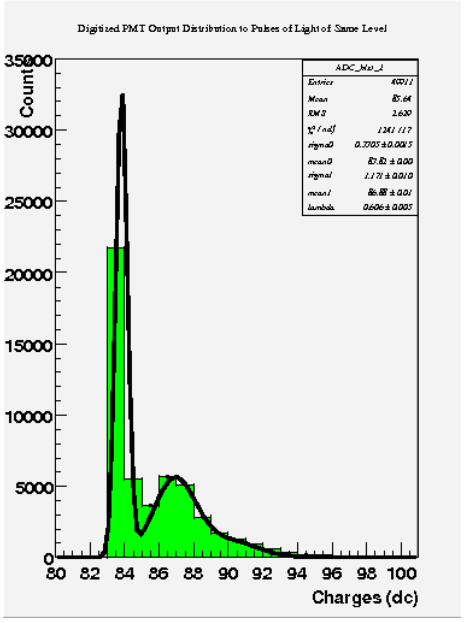

Figure 6–2: ADC output at 1600 volts using an XP2212B PMT. The multiple photoelectron fit is a sum of gaussians centered at each photoelectron mean, $N\mu$, where N = 1,2,3,4 and μ is the mean of the single photoelectron. The area of each gaussian is equal to the poissonian probability of getting N photoelectrons. The fit is used to obtain the width and mean of the single photoelectron peak.

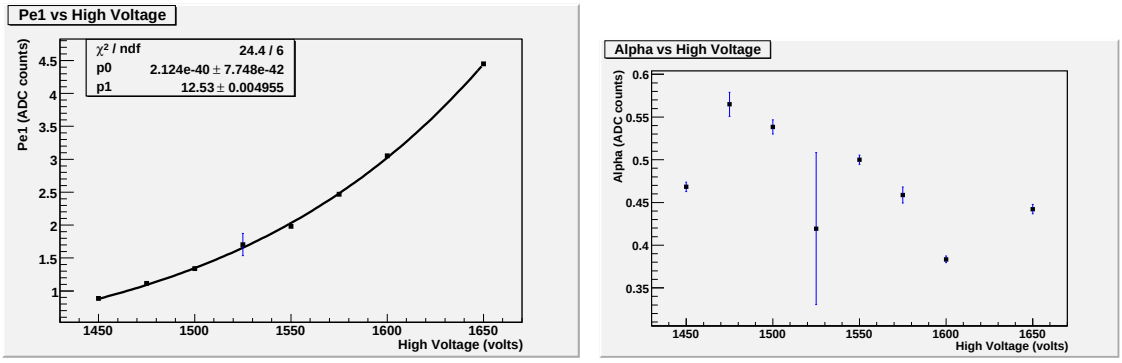

Figure 6–3: Left: Mean charge of the single photoelectron peak as a function of HV for a XP2212B PMT. The fit is of the form $\mu_{pe1} = k_\mu HV^\gamma$, where γ from the fit is 12.53 ± 0.01. Right: α, the width parameter of the single photoelectron peak plotted against HV. The large error bars at 1600 volts are the result of a poor fit.

for the XP2282B. Despite this, the single photon detection results will be outlined briefly to give a feeling for the parameter α.

First, the charge distributions of the pulses at very low light levels were plotted in a histogram (Figure 6–2). The distribution was then fit with a sum of normalized gaussians centered at each photoelectron mean ($N\mu$) where N = 1,2,3,4 ... and μ is the mean charge of the single photoelectron. Refer back to Figure 2–5 for a detailed fit of the first few photoelectrons that was done for a VERITAS PMT. The fit determines the location and width of the single photoelectron peak. Using the results from the fit, the resulting distribution of the mean charges of the single photoelectron peak and α were plotted as a function of HV (Figure 6–3).

6.2 Gain measurement

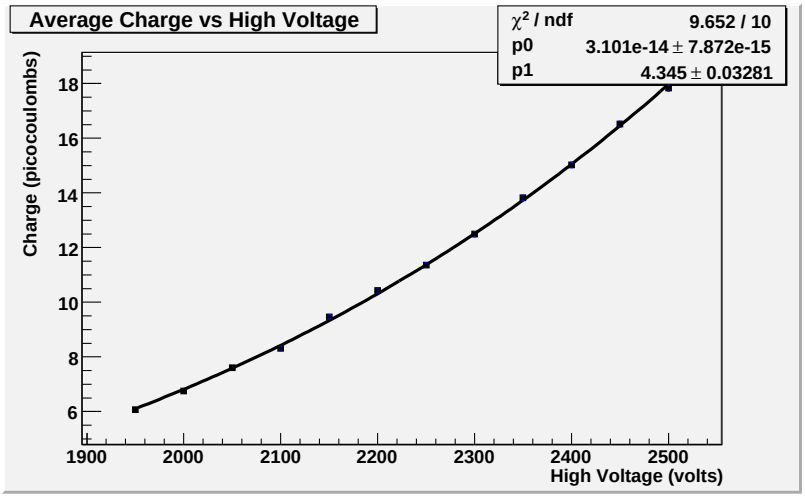

Figure 6–4: Charge of PMT signal vs HV, fit to $\mu = k_\mu HV^\gamma$, where μ is the charge, k_μ is constant and γ, also a constant, reflects the structure of the dynode chain of the PMT.

This section describes the result of calculating the gain of four PMTs (XP2282B) using different methods. The PMTs will be referred to by number (PMT 1, PMT 2 etc.). Due to the fact that single photoelectron detection was not possible for these PMTs, α was set to zero, but is in fact likely to be large. This measure will introduces some error into the calculation of the gain using method A (See Equation (3.9)). However, if one compares method A to method B, this error will decrease significantly, since only the change in α as a function of HV will contribute. Thus it is valid to compare the two methods, and to expect them to agree within a few percent of each other, a discrepancy which arises due to the ~ 10 % variation observed in α values as a function of HV, as seen in Figure 6–3.

Prior to measuring the gain of a PMT, a simple test was executed to ensure that it was in working order. An LED was pulsed at a constant light level, while the HV was changed. At each HV, 5000 pulses were integrated with an ADC, and the average charge was plotted as a function of HV (See Figure 6–4 for the results for PMT 1). Mean charge (μ) is proportional to the gain, therefore, in order to verify that the gain behaves as expected, one can simply test whether the relationship $\mu = k_\mu HV^\gamma$ is satisfied. This fit applied to the PMT 1 charges was very reasonable, demonstrating that the gain of this PMT behaves as expected.

6.3 Method A results

Method A involved reading in the charge of pulses from a PMT exposed to pulsed light at different high voltages and different light levels. At each light level and HV, the charges of the PMT signals were binned into histograms. Figure 6–5 shows an example of such histograms for PMT 1 at 2100 volts. The σ^2 vs μ of these

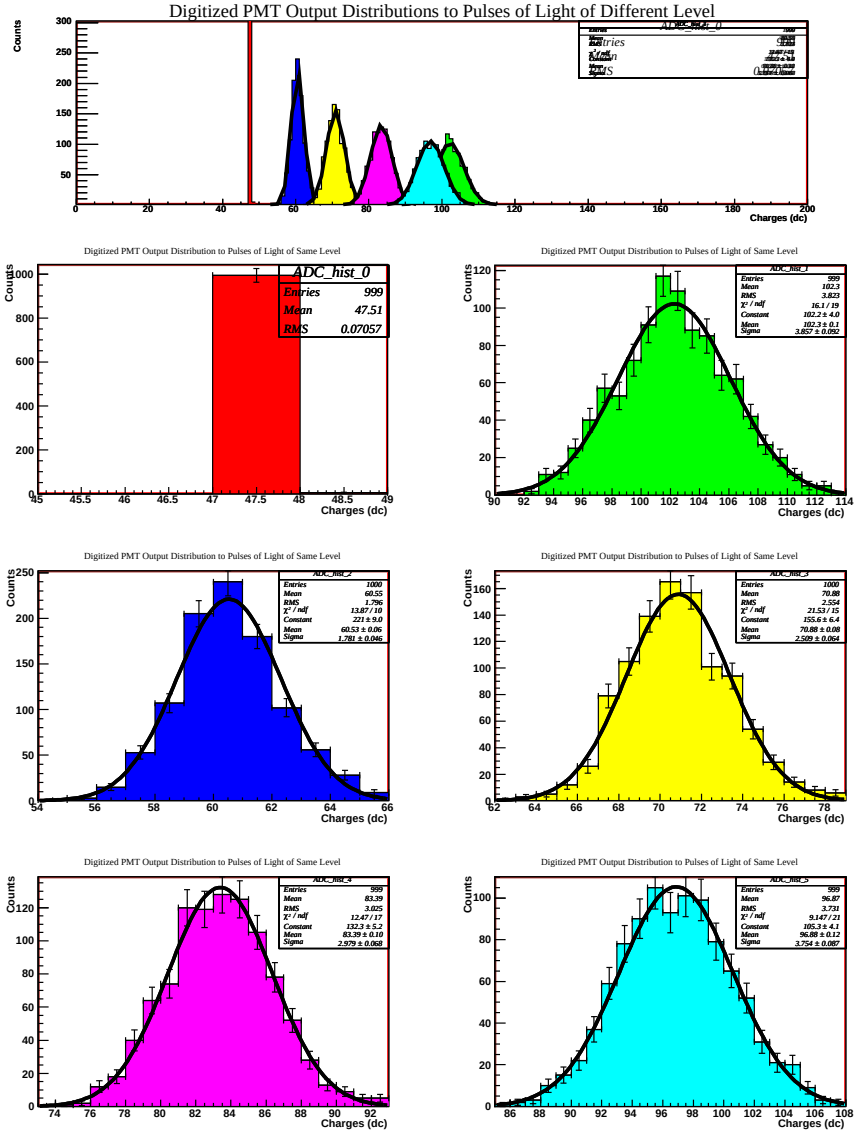

Figure 6–5: Histograms of charge distributions for PMT 1 at 2100 volts exposed to increasing light levels. The first distribution is for the PMT with the light turned off (pedestal). As the light level increases, so do μ and σ.

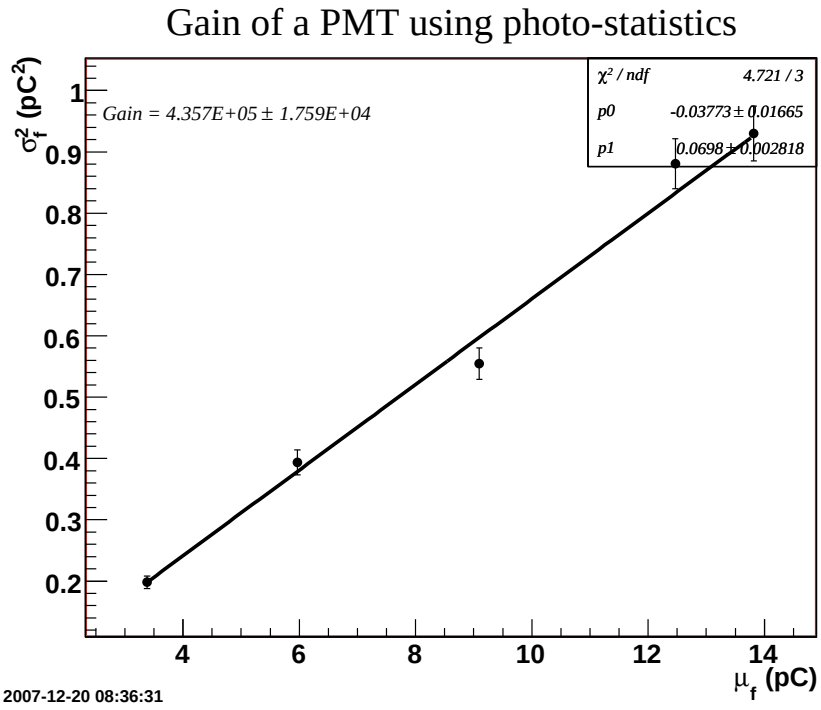

Figure 6–6: σ^2 vs μ for the charge distributions from the previous figure, for PMT 1 at 2100 volts. The gain is proportional to the slope of the line and using method A, the gain is calculated to be $4.4 \pm 0.2 \times 10^5$.

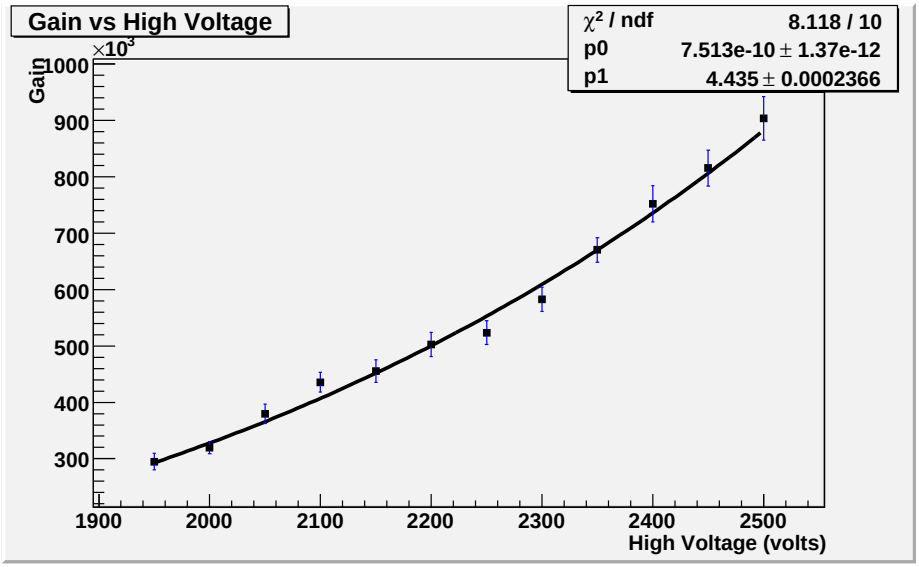

Figure 6–7: Gain calculated using method A plotted as a function of HV for PMT 1. The fit is reasonable and the γ value of 4.435 ± 0.001 agrees reasonably well with 4.34 ± 0.03, the previously measured γ.

charge distributions were then plotted and the slope was calculated (Figure 6–6). Finally, the gain was calculated by substituting these slopes into equation 3.9, but with α set to zero. These gains were then plotted as a function of HV (See Figure 6–7 for the gains of PMT 1). A power-law fit to this plot should yield approximately the same γ as was previously obtained. The two agree within a few percent, and are 4.435 ± 0.001 and 4.34 ± 0.03, respectively.

6.4 Method B results

In this method, traces were read from the oscilloscope at 10 different light levels, where the light level was constant as opposed to pulsing. Both σ^2_{FADC} and I were calculated from the trace (Figure 6–8) and plotted (Figure 6–9). The slope of σ^2_{FADC} vs I is proportional to the gain, therefore the slopes were plotted as a function of

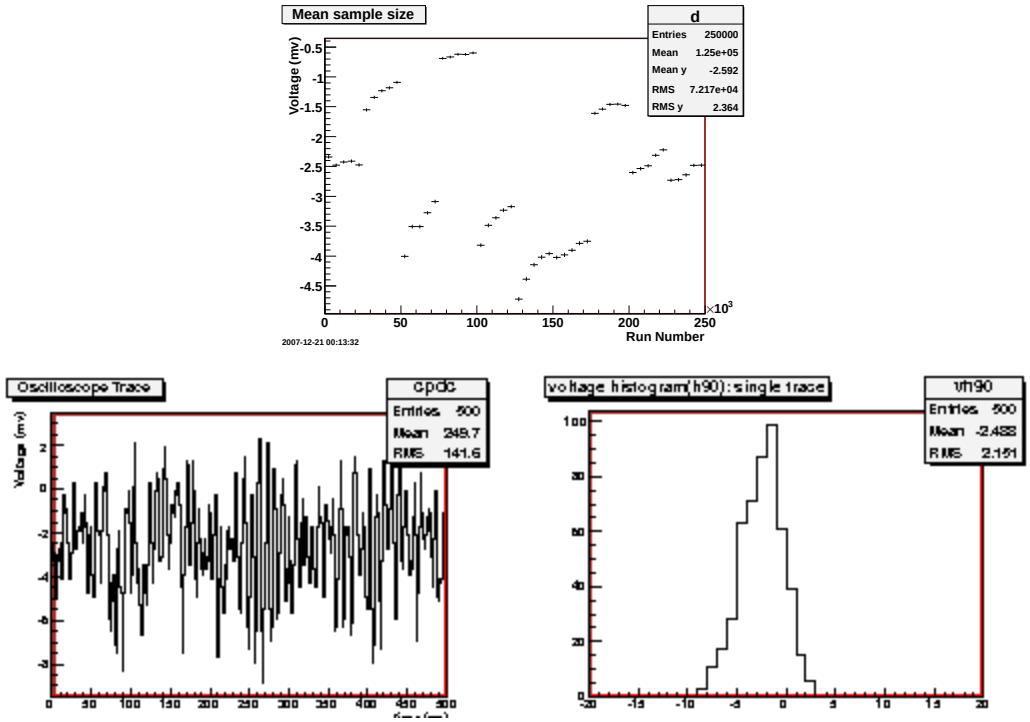

Figure 6–8: Three plots from the data of PMT 1 at 2100 volts used in method B. Top: Profile of the amplitude of the PMT signal for 10 light levels, where the light is constant and not pulsed. Note that the light level is not exactly constant over each of the 10 light levels, thus the profile breaks it down further. The amplitude of the light decreases with time as the LED approaches equilibrium, and this change effectively allows a sampling over extra light levels. Bottom Left: A sample trace as read in from the oscilloscope. Bottom Right: Histogram of the trace samples. The distribution is approximately gaussian with mean μ and variance σ^2_{FADC}.

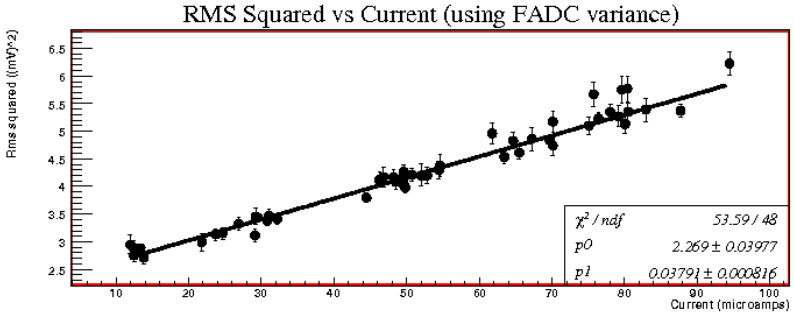

Figure 6–9: σ^2 vs I for 10 different light levels for PMT 1 at 2100 volts. Each point represents 10 ADC traces and each light level is broken up into 5 points because the light level is not very constant. The slope of the best fit was found to be .0379±0.0008. This slope is plotted in the next plot.

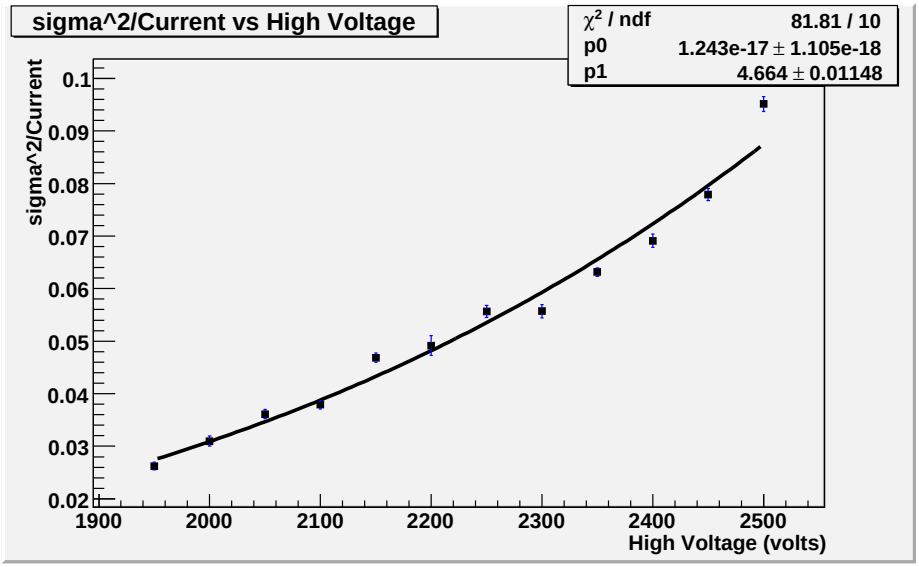

Figure 6–10: Slope of σ^2_{FADC}/I vs HV as per method B plotted as a function of HV (PMT 1). Only statistical errors are included and γ from the fit is $4.66 \pm .01$

HV and fit to a power-law (Figure 6–10). The fit is also reasonable and the power law factor agrees approximately with those in Figures 6-7 and 6-4.

6.5 Method A vs Method B

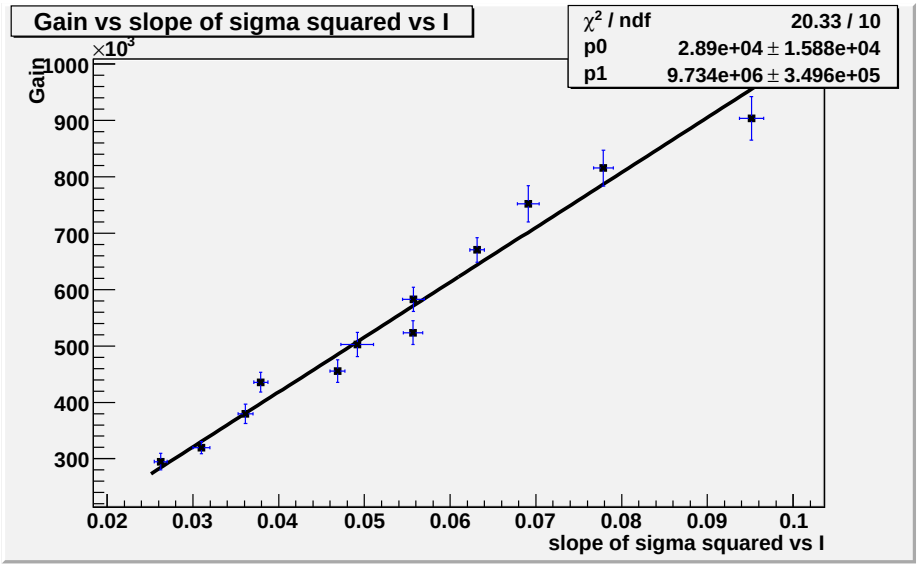

Figure 6–11: The gain calculated using method A plotted against the slope of σ^2_{FADC}/I from method B for PMT 1. The slope is $9.7 \pm 0.3 \times 10^6$.

The two methods will now be compared to determine whether both give a similar value for the gain. For PMT 1, the gain from method A was plotted against the slopes of σ^2_{FADC} vs I from method B. The relationship one expects to observe is a straight line with zero intercept, and a slope that is within a few percent of 8.26×10^7, according to equation (3.25) which states $G = \frac{1}{1.21\times10^{-8}} \frac{\sigma^2_{FADC}}{I} 1$ [1]. This slope was found to be $9.7 \pm 0.3 \times 10^6$ for PMT 1 (Figure 6–11), which is an order of magnitude

[1] $\frac{1}{1.21\times10^{-8}} = 8.26 \times 10^7$

Slope of the gain vs σ^2_{FADC}/I		
PMT#	Slope ($\times 10^6$)	Error ($\times 10^6$)
PMT 1	9.7	.3
PMT 2	9.5	.3
PMT 3	1.1	.3
Tube 4	7.6	.4
	6.9	.4

Table 6–1: Table of slopes of the gain vs σ^2_{FADC}/I for 4 PMTs. PMT 4 was repeated and both results are included. The expected slope is 8.26×10^7, which is an order of magnitude higher than the slopes observed. Furthermore, although three PMTs have slopes that agree with each other, one does not agree. It is interesting to note that the slope is directly related to the pulse shape due to an individual photoelectron.

less than the expected slope. This means that the expression for the gain in method B is not consistent with data. Furthermore, none of the other three PMTs tested agreed with the theoretical slope. Their slopes are listed in Table 6–1.

One possible explanation for this discrepancy is that the pulse shape of this PMT is different than was initially proposed. The factor relating the gain to σ^2_{FADC}/I comes directly from the pulse shape. Thus a different pulse shape should result in a different factor for the slope. However, the actual pulse shape of an individual photon was not measured for this PMT, thus this theory has not yet been tested.

The three remaining PMTs that were studied also had plots of method A vs. method B. These plots are presented in Figures 6–12, 6–13 and 6–14. The first three PMTs had slopes that agreed with other, while the fourth one did not agree. The fact that the slopes for the different PMTs do not all agree with each other means that each individual PMT would have to calibrated in order to determine the slope. This would makes this method of measuring the gain impractical for testing large numbers of similar PMTs.

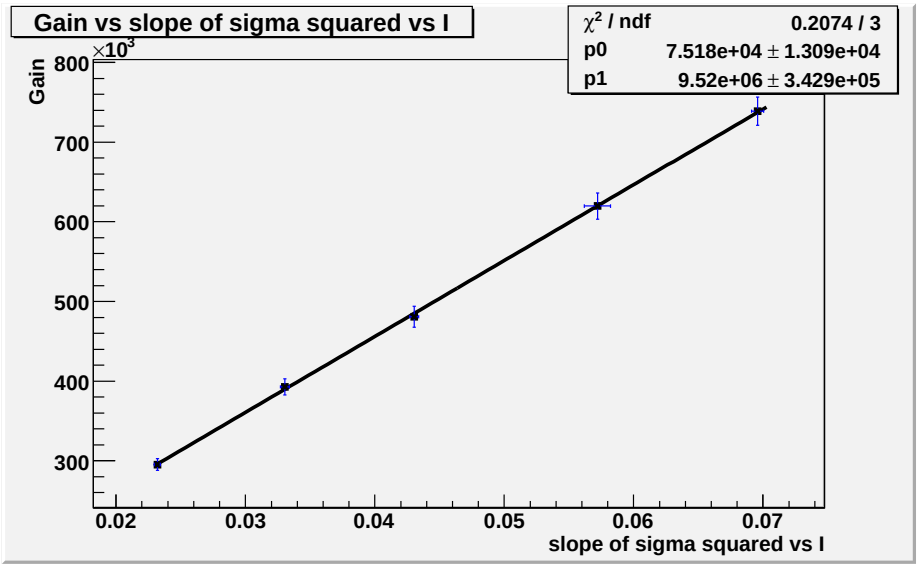

Figure 6–12: The gain calculated using method A plotted against the slope of σ^2_{FADC}/I from method B for PMT 2. The slope is $9.5 \pm 0.3 \times 10^6$.

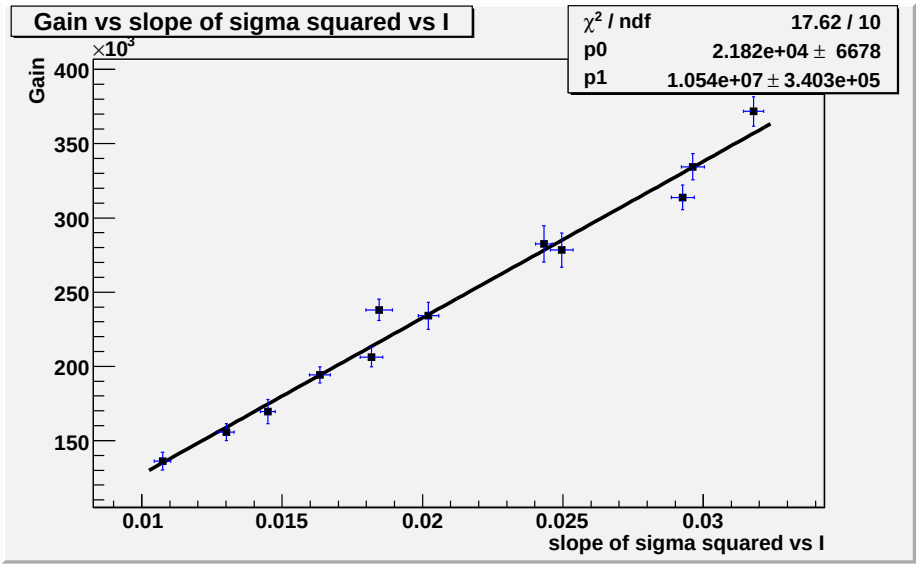

Figure 6–13: The gain calculated using method A plotted against the slope of σ^2_{FADC}/I from method B for PMT 3. The slope is $1.1 \pm 0.3 \times 10^7$.

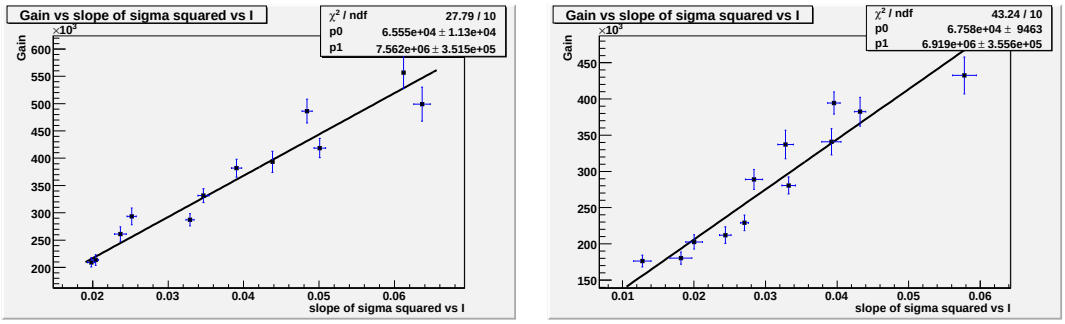

Figure 6–14: The gain calculated using method A plotted against the slope of σ^2_{FADC}/I from method B for PMT 4. The experiment was repeated and they represent the left and right plots. The slopes are $7.6 \pm 0.4 \times 10^6$ and $6.9 \pm 0.4 \times 10^6$

CHAPTER 7
Conclusion

Photomultiplier tubes (PMTs) are used to detect light coming from gamma-ray initiated showers in the earth's atmosphere. The gain of the PMTs are pivotal in determining the amount of light detected and consequently, the energy of the incoming gamma ray. In this thesis, a new method of measuring the gain of a PMT was proposed. The method was motivated mathematically, tested with experiments, and shown to work in simulations. However, when it was compared with an existing method of measuring the gain, the new method was shown to be able to predict the gain only to within a constant of multiplication. The discrepancy might be due to ignorance regarding the pulse shape of an individual photon for the PMT used. A generic pulse shape was hypothesized but it is entirely possible that it is not suitable for this particular PMT.

The best way to test this hypothesis would be to measure the pulse shape directly, or to simulate a range of possible pulse shapes in order to determine how large an effect pulse shape has. Measuring the pulse shape directly would not be possible with the XP2282B used, however, it would be possible with PMTs with better single photoelectron response. Indirect measurement of the pulse shape is also a possibility.

A major limitation of this project was the limited number of PMTs of the same type that were available. From the PMTs that were available, several showed non-ideal behaviour such as the gain not increasing with high voltage. These PMTs were immediately discarded and four remained for study. A sample size of four is not sufficient to make hard conclusions, especially in investigating why three PMTs had similar slopes for gain vs σ^2_{FADC}/I and one differed. Although the experiment was repeated in order to ascertain that the odd PMT out was not a accident, it is still possible that there is something different or malfunctioning with that single PMT. It would therefore be interesting to study more PMTs. In fact, a very large number of PMTs of the same type could potentially be studied simultaneously by using the 4 x 499 PMTs of the VERITAS gamma-ray detector and exposing them to a light source simultaneously.

The purpose of this thesis was to investigate the possibility of using a new method to measure the gains at the VERITAS detector. The main reason why this proposed method could be useful is that all of the inputs that are needed to calculate the gain are continually being read into the VERITAS data stream, in the form of current measurements and pedestal data. Using the variance of this pedestal data and plotting it against the current, one could calculate the gain using this method. These gain measurements would be taken without cutting into the time that the telescope could be observing, which is an advantage it would have over the current calibration techniques.

On a final note, as long as the constant multiplier is intrinsic to each PMT, this method could still be used to monitor the stability of the PMTs.

References

[1] T. C. Weekes. *Very high energy gamma-ray astronomy.* Very high energy gamma-ray astronomy, by Trevor C. Weekes. IoP Series in astronomy and astrophysics, ISBN 0750306580. Bristol, UK: The Institute of Physics Publishing, 2003, 2003.

[2] Ong R.A. *Very high-energy gamma-ray astronomy. Physics Reports*, 305:93–202(110), 1 November 1998.

[3] J. Holder, R. W. Atkins, H. M. Badran, G. Blaylock, S. M. Bradbury, J. H. Buckley, K. L. Byrum, D. A. Carter-Lewis, O. Celik, Y. C. K. Chow, P. Cogan, W. Cui, M. K. Daniel, I. de la Calle Perez, C. Dowdall, P. Dowkontt, C. Duke, A. D. Falcone, S. J. Fegan, J. P. Finley, P. Fortin, L. F. Fortson, K. Gibbs, G. Gillanders, O. J. Glidewell, J. Grube, K. J. Gutierrez, G. Gyuk, J. Hall, D. Hanna, E. Hays, D. Horan, S. B. Hughes, T. B. Humensky, A. Imran, I. Jung, P. Kaaret, G. E. Kenny, D. Kieda, J. Kildea, J. Knapp, H. Krawczynski, F. Krennrich, M. J. Lang, S. LeBohec, E. Linton, E. K. Little, G. Maier, H. Manseri, A. Milovanovic, P. Moriarty, R. Mukherjee, P. A. Ogden, R. A. Ong, J. S. Perkins, F. Pizlo, M. Pohl, J. Quinn, K. Ragan, P. T. Reynolds, E. T. Roache, H. J. Rose, M. Schroedter, G. H. Sembroski, G. Sleege, D. Steele, S. P. Swordy, A. Syson, J. A. Toner, L. Valcarcel, V. V. Vassiliev, S. P. Wakely, T. C. Weekes, R. J. White, D. A. Williams, and R. Wagner. *The First VERITAS Telescope. Astroparticle Physics*, 25:391, 2006.

[4] T. C. Weekes. *VERITAS: the Very Energetic Radiation Imaging Telescope Array System. Astroparticle Physics*, 17:221, 2002.

[5] Maxim Integrated Products, Dallas Semiconductor. *Understanding Flash ADCs*, October 2001. Application Note: 810.

[6] David Hanna. *Calibration Techniques for VERITAS.* Proc. 30th ICRC, 2007.

[7] Flyckt, Esso and Marmonier, Carole, editor. *Photomultiplier Tubes Principles and Applications.* Photonis, 2002.

[8] M. Garcia-Munoz, G. M. Mason, and J. A. Simpson. *The age of the galactic cosmic rays derived from the abundance of Be-10.* ApJ, 217:859–877, November 1977.

[9] J. A. Simpson. *Elemental and Isotopic Composition of the Galactic Cosmic Rays. Annual Review of Nuclear and Particle Science*, 33:323–382, 1983.

[10] M. Harwit. *Cosmic Discovery.* Cosmic Discovery, by Martin Harwit, pp. 346. ISBN 0-262-58068-3. Cambridge, Massachusetts, USA: The MIT Press, April 1984. (Paper), April 1984.

[11] E. Fermi. *On the Origin of the Cosmic Radiation. Physical Review*, 75:1169–1174, April 1949.

[12] V. L. Ginzburg and S. I. Syrovatskii. *The Origin of Cosmic Rays.* The Origin of Cosmic Rays, New York: Macmillan, 1964, 1964.

[13] R. Blandford and D. Eichler. *Particle Acceleration at Astrophysical Shocks - a Theory of Cosmic-Ray Origin.* Phys. Rep., 154:1–+, October 1987.

[14] W. I. Axford. *The origins of high-energy cosmic rays.* ApJS, 90:937–944, February 1994.

[15] R. D. Blandford and J. P. Ostriker. *Particle acceleration by astrophysical shocks.* ApJ, 221:L29–L32, April 1978.

[16] P. O. Lagage and C. J. Cesarsky. *The maximum energy of cosmic rays accelerated by supernova shocks.* A&A, 125:249–257, September 1983.

[17] H. J. Voelk and P. L. Biermann. *Maximum energy of cosmic-ray particles accelerated by supernova remnant shocks in stellar wind cavities.* ApJ, 333:L65–L68, October 1988.

[18] A. M. Hillas. *The Origin of Ultra-High-Energy Cosmic Rays.* ARA&A, 22:425–444, 1984.

[19] Philip Morrison. *On the Origins of Cosmic Rays. Rev. Mod. Phys.*, 29(2):235–243, Apr 1957.

[20] T. C. Weekes. *Very high energy gamma-ray astronomy. Physics Reports*, 160:1–2, March 1988.

[21] G. Cocconi. *Proc. 6th ICRC.* volume 2, page 309, 1959.

[22] G. G. Fazio, H. F. Helmken, G. H. Rieke, and T. C. Weekes. *A Search for Discrete Sources of Cosmic Gamma Rays of Energies Near* 2×10^{12} *eV.* ApJ, 154:L83+, November 1968.

[23] P. V. Ramana Murthy and A. W. Wolfendale. *Gamma-ray Astronomy.* Cambridge University Press, May 1993.

[24] C. E. Fichtel, R. C. Hartman, D. A. Kniffen, D. J. Thompson, H. Ogelman, M. E. Ozel, T. Tumer, and G. F. Bignami. *High-energy gamma-ray results from the second small astronomy satellite.* ApJ, 198:163–182, May 1975.

[25] B. N. Swanenburg et al. *SECOND COS B CATALOG OF HIGH-ENERGY GAMMA-RAY SOURCES. Astrophys. J.*, 243:L69–L73, 1981.

[26] T. C. Weekes and K. E. Turver. *Gamma-ray astronomy from 10-100 GeV: A new approach.* In R. D. Wills and B. Battrick, editors, *Recent Advances in Gamma-Ray Astronomy*, volume 124 of *ESA Special Publication*, pages 279–286, July 1977.

[27] T. C. Weekes, M. F. Cawley, D. J. Fegan, K. G. Gibbs, A. M. Hillas, P. W. Kowk, R. C. Lamb, D. A. Lewis, D. Macomb, N. A. Porter, P. T. Reynolds, and G. Vacanti. *Observation of TeV gamma rays from the Crab nebula using the atmospheric Cerenkov imaging technique.* ApJ, 342:379–395, July 1989.

[28] W. N. Johnson, R. L. Kinzer, J. D. Kurfess, M. S. Strickman, W. R. Purcell, D. A. Grabelsky, M. P. Ulmer, D. A. Hillis, G. V. Jung, and R. A. Cameron. *The Oriented Scintillation Spectrometer Experiment - Instrument description.* ApJS, 86:693–712, June 1993.

[29] *CGRO Science Support Center.* http://cossc.gsfc.nasa.gov/docs/cgro/index.html.

[30] R. A. Ong. *The Status of VHE Gamma-Ray Astronomy. ArXiv Astrophysics e-prints*, May 2006.

[31] A. M. Hillas, C. W. Akerlof, S. D. Biller, J. H. Buckley, D. A. Carter-Lewis, M. Catanese, M. F. Cawley, D. J. Fegan, J. P. Finley, J. A. Gaidos, F. Krennrich, R. C. Lamb, M. J. Lang, G. Mohanty, M. Punch, P. T. Reynolds, A. J. Rodgers, H. J. Rose, A. C. Rovero, M. S. Schubnell, G. H. Sembroski, G. Vacanti, T. C. Weekes, M. West, and J. Zweerink. *The Spectrum of TeV Gamma Rays from the Crab Nebula.* ApJ, 503:744–+, August 1998.

[32] S. F. Taylor, T. Abu-Zayyad, K. Belov, Z. Cao, G. Chen, M. A. Huang, C. C. H. Jui, D. B. Kieda, E. C. Loh, J. N. Matthews, M. Salamon, A. Salman, J. D. Smith, P. Sokolsky, P. Sommers, S. B. Thomas, L. R. Wiencke, D. J. Bird, R. W. Clay, B. R. Dawson, K. M. Simpson, C. R. Wilkinson, J. Boyer, E. J. Mannel, Y. Ho, W. Lee, T. O'Halloran, N. Hayashida, H. Hirasawa, F. Ishikawa, H. Lafoux, M. Nagano, D. Nishikawa, T. Ouchi, H. Ohoka, M. Ohnishi, N. Sakaki, M. Sasaki, H. Shimodaira, M. Teshima, R. Torii, T. Yamamoto, S. Yoshida, and T. Yuda. *The Highest Energy Cosmic Rays and Gamma Rays*. In *Bulletin of the American Astronomical Society*, volume 30 of *Bulletin of the American Astronomical Society*, pages 827–+, May 1998.

[33] W. Hofmann. *H.E.S.S. Status*. In *Towards a Network of Atmospheric Cherenkov Detectors VII*, pages 43–56, 2005.

[34] David Hanna. *VERITAS Telescopes Celebrate First Light. CERN Cour.*, 2007.

[35] J. Holder and The VERITAS collaboration. *VERITAS: Status and Performance*, 2006.

[36] John M. Davies and Eugene S. Cotton. *Design of the quartermaster solar furnace. Solar Energy*, 1:16–22, 1957.

[37] V. V. Vassiliev, J. Hall, D. B. Kieda, J. Moses, T. Nagai, and J. Smith. *Veritas CFDs*. In *International Cosmic Ray Conference*, volume 5 of *International Cosmic Ray Conference*, pages 2851–+, July 2003.

[38] J. Holder and for the VERITAS Collaboration. *Status and Performance of the First VERITAS telescope*, 2005.

[39] D Hanna and R. Mukherjee. *The laser calibration system for the STACEE ground-based gamma ray detector. Nuclear Instruments and Methods in Physics Research Section A: Accelerators, Spectrometers, Detectors and Associated Equipment*, 482(1-2):271–280, 2002.

[40] G. Vacanti, P. Fleury, Y. Jiang, E. Paré, A. C. Rovero, X. Sarazin, M. Urban, and T. C. Weekes. *Muon ring images with an atmospheric Čerenkov telescope. Astroparticle Physics*, 2:1–11, February 1994.

[41] David Hanna. *A New Way to Monitor Phototube Gain in STACEE*, STACEE Note 03-04.

[42] Philip R. Bevington et al. *Data Reduction and Error Analysis for the Physical Sciences*. McGraw-Hill, 2nd edition, 1992.

[43] Francis J. Lombard and Fred Martin. *Statistics of Electron Multiplication. Review of Scientific Instruments*, 32(2):200–201, 1961.

[44] Jean-Phillipe Gagnon. *An instrument to study the photon flux from the night sky in the wavelength region relevant for atmospheric cherenkov telescopes*, 2005.

[45] D.M. et al. Gingrich. *The STACEE ground-based gamma-ray detector. Nuclear Science, IEEE Transactions on*, 52(6):2977–2985, Dec. 2005.

[46] *LeCroy Research Systems Corporation. CAMAC Model 2249W 12 Channel Analog-to-Digital Converter.* 700 South Main Street, Spring Valley, N.Y. 10977, 1984.

[47] *http://root.cern.ch/.*